CHAPTER III

RESULTS

3.1 Generation and identification of *Prx1*-Cre/*Vcan*$^{flox/flox}$ mice

3.1.1 Generation of *Prx1*-Cre/*Vcan*$^{flox/flox}$ mice

A conditional targeting vector for the versican gene *Vcan*, in which exon 2 was flanked by the *loxP* sequence, was designed as shown in figure 3.1. The targeting vector also contained a PGK-neo^{R} cassette flanked by the FRT sequence. Regarding to the Flp/FRT recombination system, it is known to be essential in utilization for the eukaryotic homolog of the Cre/*loxP* system (233). Flp is a monomeric peptide consisting 423 amino acid, and is similar to Cre. FRT is similar to *loxP* in that it is composed of three 13-bp repeats surrounding an 8-bp asymmetric spacer region. Although not as widely used as Cre/*loxP*, the Flp/FRT system has been shown to cause site-specific DNA recombination in ES cells and transgenic mice (234). Despite similar mechanisms of action and DNA recognition sites, the Cre/*loxP* and Flp/FRT systems do not exhibit significant cross-reactivity (235). Therefore, Flp/FRT system was applied to remove the selectable marker in this study.

The schematic representing for generation of transgenic mice was demonstrated in figure 3.2. For gene targeting in ES cells, the cells were firstly transfected with the vector. After selection with G418 and screening by genomic PCR and southern blot analysis, five ES cell clones with homologous recombination were collected for generation of chimeric mice by blastocyst injection. The chimeric mice were crossed with wild-type mice, and offspring mice with germ line transmission were obtained.

Next, to remove PGKneo^{R} cassette, the mice were crossed with CAG-flippase Tg mice, and *Vcan*$^{+/flox}$ mice whose genomic DNA lacks the PGK-neo^{R} cassette were obtained. These mice were back-crossed with C57BL/6 mice to segregate the CAG-flippase transgene and further back-crossed to C57BL/6 mice at least four times (N≥4). Then, *Vcan*$^{flox/flox}$ mice were generated by crossing *Vcan*$^{+/flox}$ male and female mice. Both *Vcan*$^{+/flox}$ mice and *Vcan*$^{flox/flox}$ mice were healthy and fertile. Next, *Vcan*$^{+/flox}$ mice were then crossed with *Prx1*-Cre Tg mice with the background of C57BL/6, and *Prx1*-Cre/*Vcan*$^{+/flox}$ mice were obtained. Versican is transiently expressed at a high level in the mesenchymal condensation areas of cartilage primordium. There, a transcription factor, *Prx-1*, is also expressed at a high level (34). *Prx1*-Cre/*Vcan*$^{+/flox}$ male and female mice were crossed to obtain *Prx1*-Cre/*Vcan*$^{flox/flox}$ mice whose *Vcan* gene was removed by Cre-mediated excision in the mesenchymal condensation areas, where Prx1 promoter activity is present.

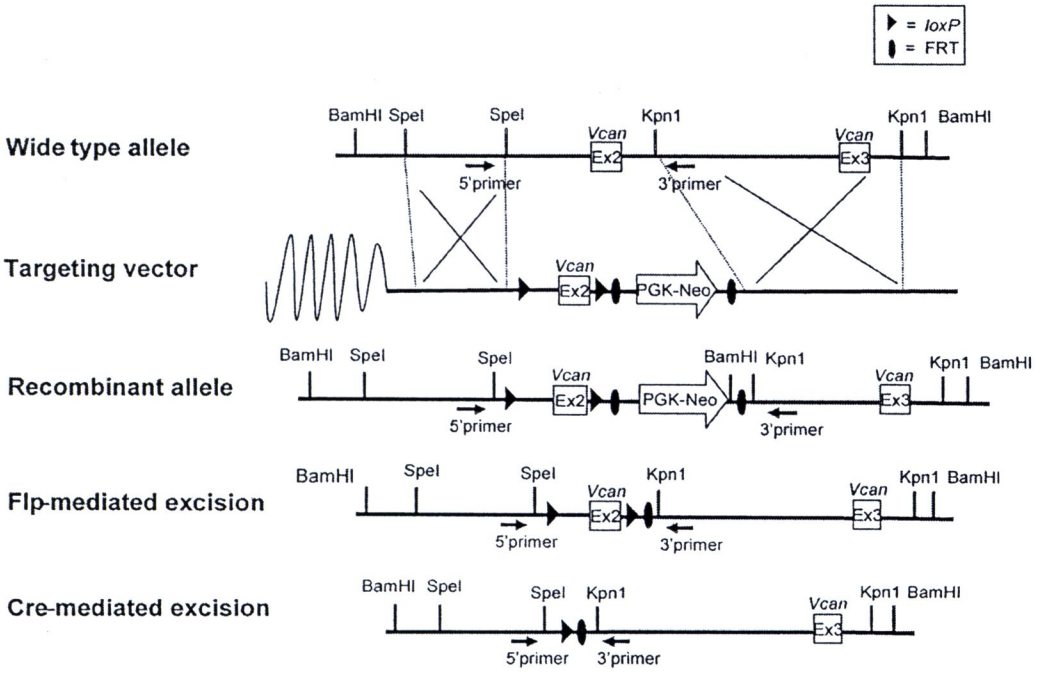

Figure 3.1 Genomic construct for conditional deletion of the *Vcan* mice. The wild-type *Vcan* locus is depicted on the *top line*. A *Vcan* targeting vector was constructed by flanking exon 2 with *loxP* sites and flanking a PGK-neo^R cassette with FRT sites (*Targeting vector*). ES cells clones with homologous recombination of the vector segment (*Recombinant allele*) were obtained by positive selection and used for generation of chimera mice, followed by germ line transmission. The FRT-flanked PGK- neo^R cassette was subsequently deleted from the recombinant allele by crossing with CAG-Flp Tg mice. These mice, termed *Vcan*$^{flox/flox}$, were crossed with *Prx1*-Cre Tg mice. These mice have cells with the null allele of *Vcan*, in regions where *Prx1* promoter is and was active.

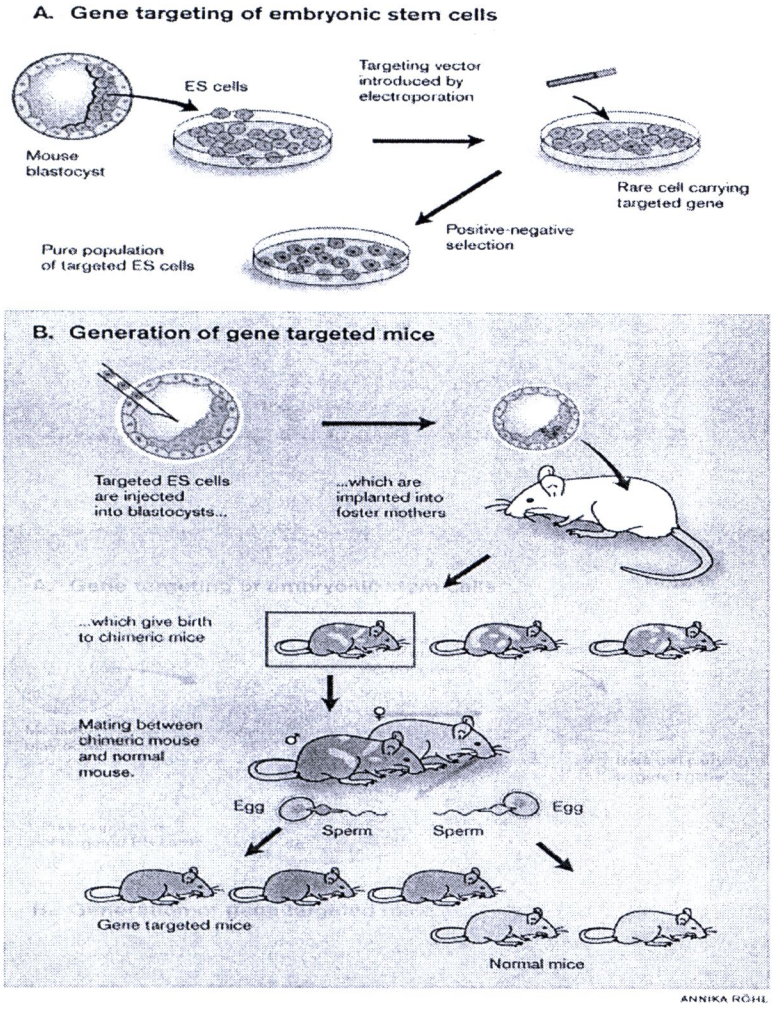

Figure 3.2 Illustration of the generation of transgenic mice. (A) Gene targeting for ES cells. (B) Generation of gene targeted mice (236).

3.1.2 Genotyping

3.1.2.1 Genotyping of versican transgenic mice

The genotyping of transgenic mice was performed by PCR using DNA template from proteinase K digestion of tail biopsy as described in materials and methods. WT and floxed alleles were identified by PCR using a forward primer of Int1-1 and a reverse primer of Kpn-1, generating a PCR product of 3kb in WT and 2kb in floxed alleles.

3.1.2.2 Genotyping of *Prx1*-Cre mice

DNA template was prepared by tail biopsy. PCR for Cre transgene was performed using the following primer set of Prx1-Cre forward and Prx1-Cre reverse, which generated a PCR product of 620 bp.

The genotyping of Cre, *Vcan*, and floxed alleles are shown in figure 3.3. In WT or *Prx1*-Cre/*Vcan*$^{+/+}$ mouse, there was a band of WT allele at 3 kb, in heterozygous or *Prx1*-Cre/*Vcan*$^{+/flox}$ mouse, there were two bands at 2 kb and 3 kb of floxed and WT alleles, respectively. In homozygous or *Prx1*-Cre /*Vcan*$^{flox/flox}$ mouse, there was a band of floxed allele at 2 kb. All of these mice contained *Prx1*-Cre transgene as appeared in the lowest bands at 620 kb.

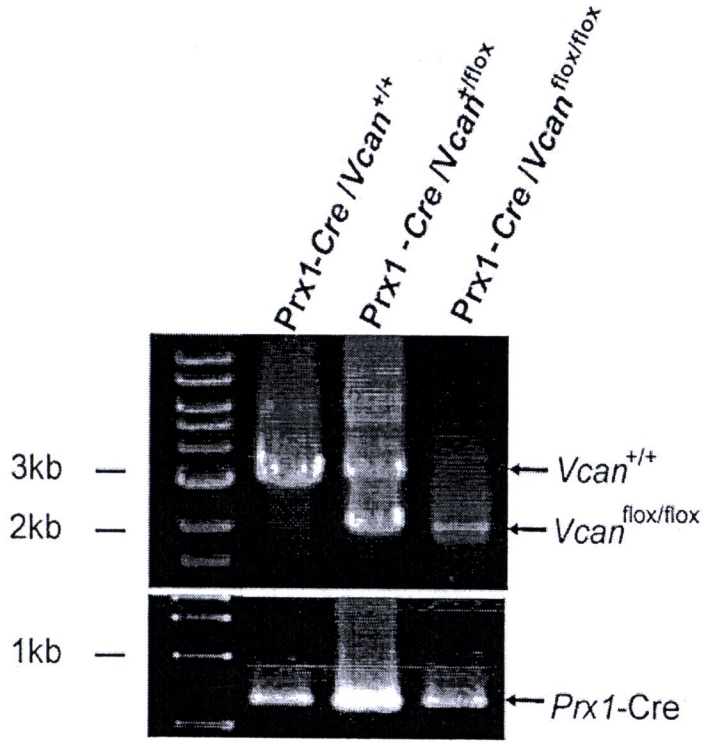

Figure 3.3 Genotyping of *Prx1*-Cre/*Vcan*$^{+/+}$, *Prx1*-Cre/*Vcan*$^{+/flox}$, and *Prx1*-Cre/*Vcan*$^{flox/flox}$ mice. The PCR analysis was performed on genomic DNA prepared from a tail biopsy. The WT (*Vcan*$^{+/+}$) PCR product is 3 kb, and the *flox* (*Vcan*$^{flox/flox}$) product without PGK-neo^{R} cassette is 2 kb. The *Prx1*-Cre transgene was detected by PCR using another primer set. The reaction product (~620 bp) is shown.

3.1.3 DNA sequencing

To confirm whether the 2kb of floxed band contained floxed allele, it was further identified by DNA sequencing. The sequencing was done according to materials and methods, and sample which contained floxed allele was used to enlarge scale by PCR, figure 3.4. The 2 kb of floxed allele without PGK-neo^{R} cassette was then purified for DNA sequencing. The sequencing data were extracted and analyzed using BLAST analysis tool on NCBI mouse DNA database, the sequence was subsequently identified. As depicted in figure 3.1, after PGK-neo^{R} cassette was deleted from the recombinant allele by Flp mediated-excision, the floxed allele should, nevertheless, contain *loxP*. DNA sequence was blasted to nucleotide database, the results revealed the identity sequence related to *Mus musculus* chromosome 13 genomic contig, and all blast hits were identified as *Vcan* (the former called *Cspgs2*), displayed in table 3.1 and 3.2. Moreover, by using 001 forward and 002 reverse primers, the DNA chromatograms were clearly confirmed the present of *loxP* as shown in figure 3.5-3.7. Collectively, these results will be used for selecting *Prx1*-Cre/*Vcan*$^{+/+}$, *Prx1*-Cre/*Vcan*$^{+/flox}$, and *Prx1*-Cre/*Vcan*$^{flox/flox}$ mice, or embryos in the next experiments.

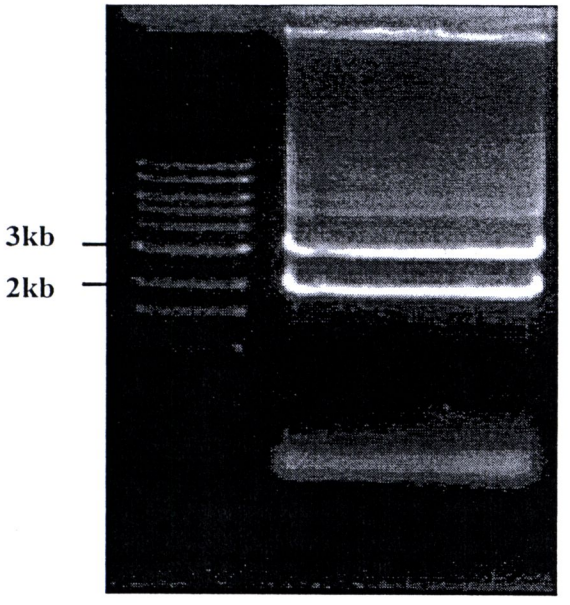

Figure 3.4 PCR analysis of *Prx1*-Cre/*Vcan*$^{+/flox}$ mice. The enlarged-PCR product of *Prx1*-Cre/*Vcan*$^{+/flox}$ shows the WT (*Vcan*$^{+/+}$) PCR product at 3 kb, and the *flox* (*Vcan*$^{flox/flox}$) product without PGK-neo^{R} cassette at 2 kb.

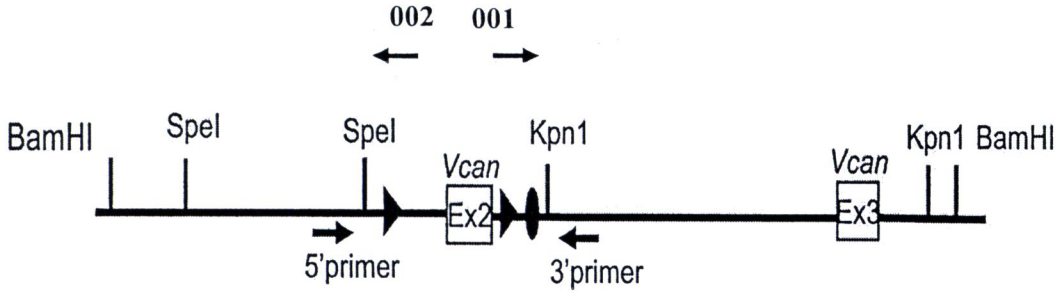

Figure 3.5 Schematic representation for primer alignment of floxed allele (*Vcan*$^{flox/flox}$). The 001 forward and 002 reverse primers were designed to anneal and amplify forward and backward of exon2 sequence, respectively.

Table 3.1 Alignment-hit table of nucleotide sequence using primer 001. Query ID; lcl|53103, query length; 829.

Blast Hits	Accession	Description	Features in this part of subject sequence	% identity
1	NT_039589.7	Mm13_39629_37	chondroitin sulfate proteoglycan 2 (*Cspg2*)	100
2	NT_039589.7	Mm13_39629_37	chondroitin sulfate proteoglycan 2 (*Cspg2*)	100
3	NT_039589.7	Mm13_39629_37	chondroitin sulfate proteoglycan 2 (*Cspg2*)	100
4	NW_001030534.1	Mm13_11175873_37	chondroitin sulfate proteoglycan 2 (*Cspg2*)	98.63
5	NW_001030534.1	Mm13_11175873_37	chondroitin sulfate proteoglycan 2 (*Cspg2*)	95

Table 3.2 Alignment-hit table of nucleotide sequence using primer 002. Query ID; lcl|879, query length; 911.

Blast Hits	Accession	Description	Features in this part of subject sequence	% identity
1	NT_039589.7	Mm_13_39629_37	chondroitin sulfate proteoglycan 2 (*Cspg2*)	100
2	NT_039589.7	Mm_13_39629_37	chondroitin sulfate proteoglycan 2 (*Cspg2*)	100
3	NW_001030534.1	Mm13_11175873_37	chondroitin sulfate proteoglycan 2 (*Cspg2*)	100
4	NW_001030534.1	Mm13_11175873_37	chondroitin sulfate proteoglycan 2 (*Cspg2*)	100

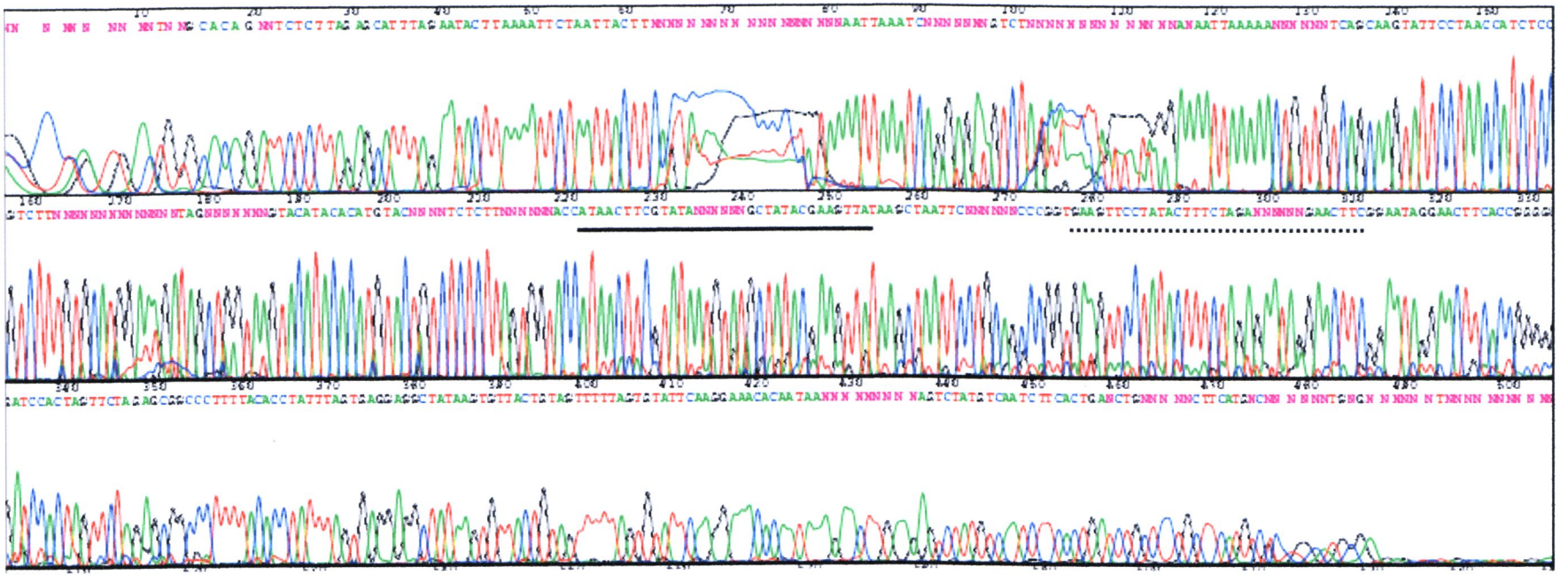

Figure 3.6 DNA sequencing using 001 forward primer generated a four-color chromatogram. A dense line represents *loxP* sequence, and a dash line represents FRT sequence of the floxed allele.

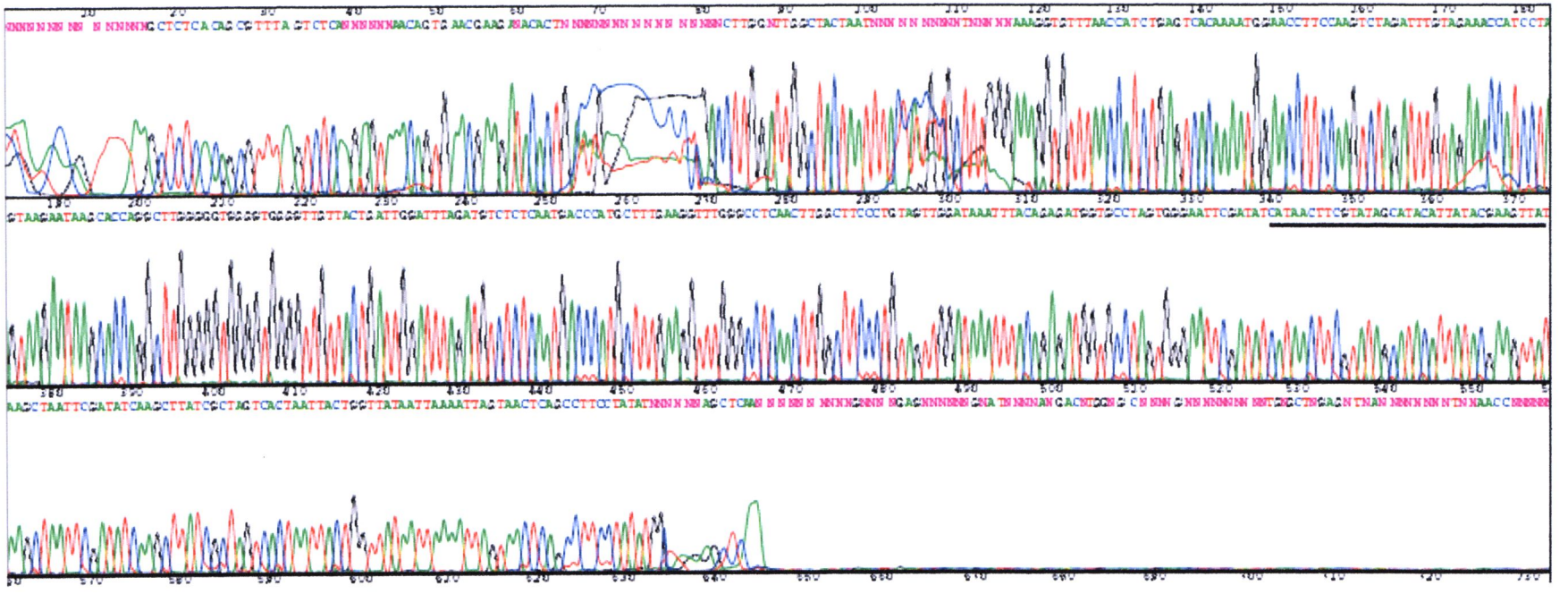

Figure 3.7 DNA sequencing using 002 reverse primer generated a four-color chromatogram. A dense line represents *loxP* sequence of the floxed allele.

Prx1-Cre/*Vcan*$^{flox/flox}$ mice grew apparently normal by gross appearance and were fertile but all of them displayed distorted digits in the limbs. To gain insight what was responsible for limb deformity, detailed studies of the limbs were examined.

3.2 Phenotype investigations reveal distortion digits found in *Prx1*-Cre/*Vcan*$^{flox/flox}$ mice

3.2.1 X-ray examination

Initially, X-ray examination of adult mice was performed. The X-ray examination revealed distortion of bones, especially in the proximal phalanges as displayed in figure 3.8.

3.2.2 Gross observation

Next, the mice at the earlier lifetime of 1 month, 2 week, 1 week of age, and at newborn were observed. By gross observation of 1-month-old, 2-week-old, and 1-week-old of *Prx1*-Cre/*Vcan*$^{+/+}$ and *Prx1*-Cre/*Vcan*$^{flox/flox}$ mice as demonstrated in figure 3.9, it was not obvious difference in the size between *Prx1*-Cre/*Vcan*$^{+/+}$ and *Prx1*-Cre/*Vcan*$^{flox/flox}$ mice. However, when they were closely observed, *Prx1*-Cre/*Vcan*$^{flox/flox}$ mice displayed the distortion in hind limbs which became obvious as early as 1-2 week of age, and was accompanied with limb shortening, figure 3.10. In contrast, the distortion was not apparent in the fore limbs and in hind limbs of newborn by gross appearance, figure 3.10.

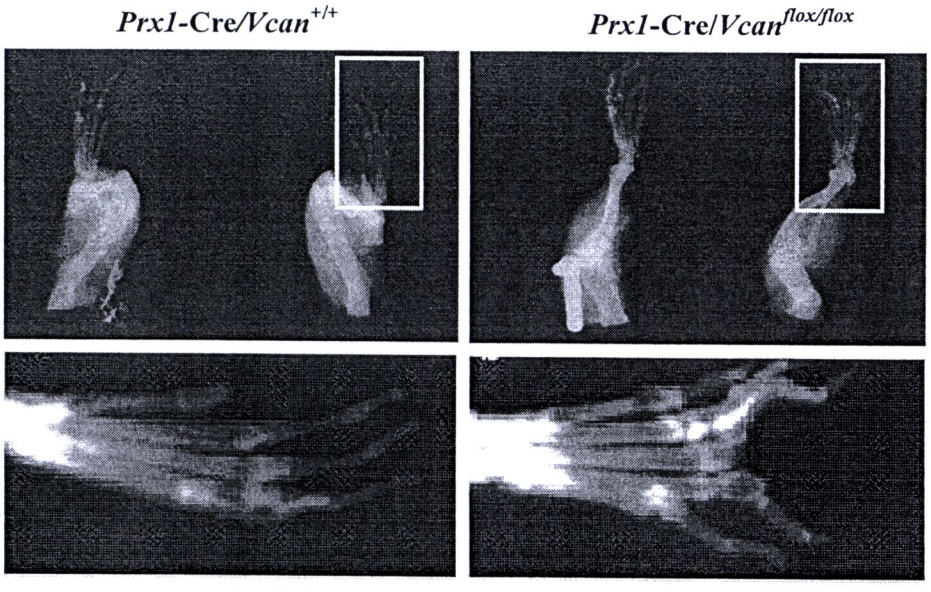

Figure 3.8 X-ray visualization of 8-month-old mice. *Prx1*-Cre/*Vcan*$^{flox/flox}$ mice (*B* and *D*) show distortion and shortening of digits, compared with *Prx1*-Cre/*Vcan*$^{+/+}$ mice (*A* and *C*), *C* and *D* as an *enlarged image* of the *boxed area* in *A* and *B*.

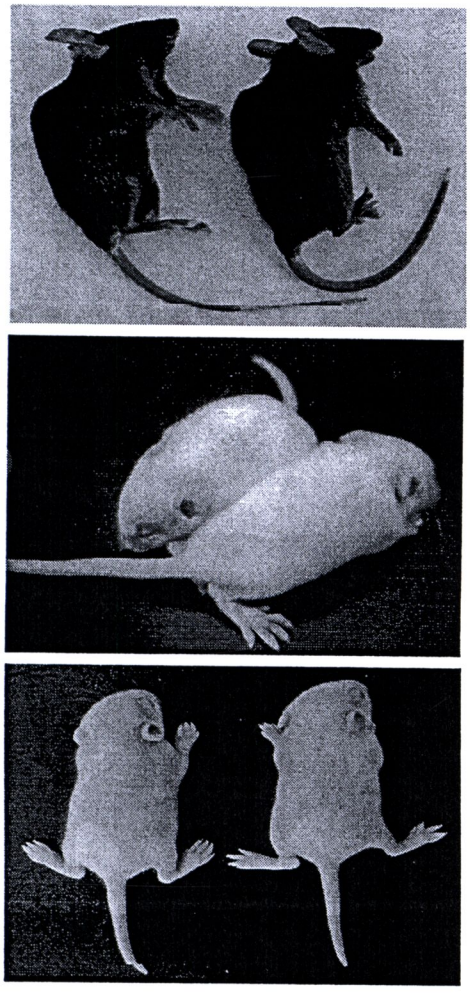

Figure 3.9 Gross observation of 1-month-old (*top*), 2-week-old (*middle*), and 1-week-old (*bottom*) of *Prx1*-Cre/*Vcan*$^{+/+}$ and *Prx1*-Cre/*Vcan*$^{flox/flox}$ mice. It is not obvious difference in the size between *Prx1*-Cre/*Vcan*$^{+/+}$ and *Prx1*-Cre/*Vcan*$^{flox/flox}$ mice.

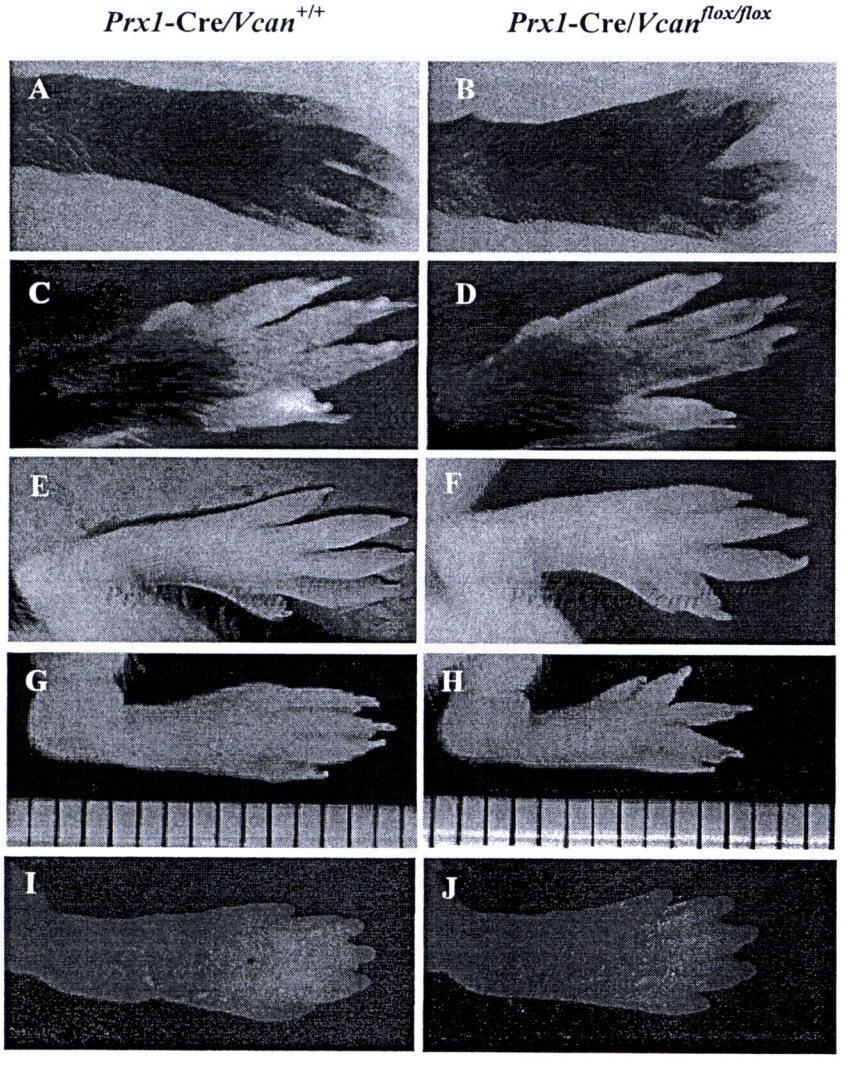

Figure 3.10 Gross observation of *Prx1*-Cre/*Vcan*$^{+/+}$ (*A, C, E, G* and *I*) and *Prx1*-Cre/*Vcan*$^{flox/flox}$ (*B, D, F , H* and *J*) hind limbs (*A, B, E, F, G, H, I* and *J*), and fore limbs (*C* and *D*). At one month of age (*A, B, C,* and *D*), *Prx1*-Cre/*Vcan*$^{flox/flox}$ mice show distortion in hind limbs (*B*) compared with *Prx1*-Cre/*Vcan*$^{+/+}$ (*A*), whereas there is not a certain deviation between *Prx1*-Cre/*Vcan*$^{+/+}$ and *Prx1*-Cre/*Vcan*$^{flox/flox}$ in fore limbs (*C* and *D*). At 2-week-old (*E* and *F*) and 1-week-old (*G* and *H*) of *Prx1*-Cre/*Vcan*$^{+/+}$ (*E* and *G*) and *Prx1*-Cre/*Vcan*$^{flox/flox}$ (*F* and *H*) mice, *Prx1*-Cre/*Vcan*$^{flox/flox}$

hind limbs (*F* and *H*) show distortion and shortening of digits, compared with *Prx1*-Cre/*Vcan*$^{+/+}$ hind limbs (*E* and *G*). However, newborn of *Prx1*-Cre/*Vcan*$^{flox/flox}$ mice (*J*) do not appear different in hind limbs, when compared with *Prx1*-Cre/*Vcan*$^{+/+}$ (*I*).

3.2.3 Histological analyses

3.2.3.1 *Prx1*-Cre/*Vcan*$^{flox/flox}$ mice exhibit delayed cartilage development at newborn

The distortion might have derived from abnormality of bone, cartilage, ligament, and tendon. To determine which region was responsible for the phenotype, histological analyses were performed. As demonstrated in figure 3.11, newborn hind limbs of *Prx1*-Cre/*Vcan*$^{+/+}$ mice showed good alignment of metatarsus and phalanges, which contained a well organized structure of differentiating chondrocytes. In contrast, *Prx1*-Cre/*Vcan*$^{flox/flox}$ mice showed distorted digits, which contained nodules of hypertrophic chondrocytes surrounded by proliferative and prehypertrophic chondrocytes. The joint surface between phalanges was tilted (*arrow*), presumably due to altered orientation of chondrocyte columns. In addition, the proximal region of proximal phalanges, adjacent to the metatarsophalangeal (*MP*) joint, exhibited cleft formation (*arrowhead*). These abnormalities were observed with complete penetrance in more than 48 mutant mice examined.

Although gross observations did not disclose abnormalities in forelimbs, as demonstrated in figure 3.12, histological analyses revealed aberrant nodules of hypertrophic chondrocytes in digits and tilting and clefting of the metacarpophalangeal joint, similar to that in hind limbs. Because the deformity was more obvious in hind limbs, hind limbs were used to investigate for further experiments.

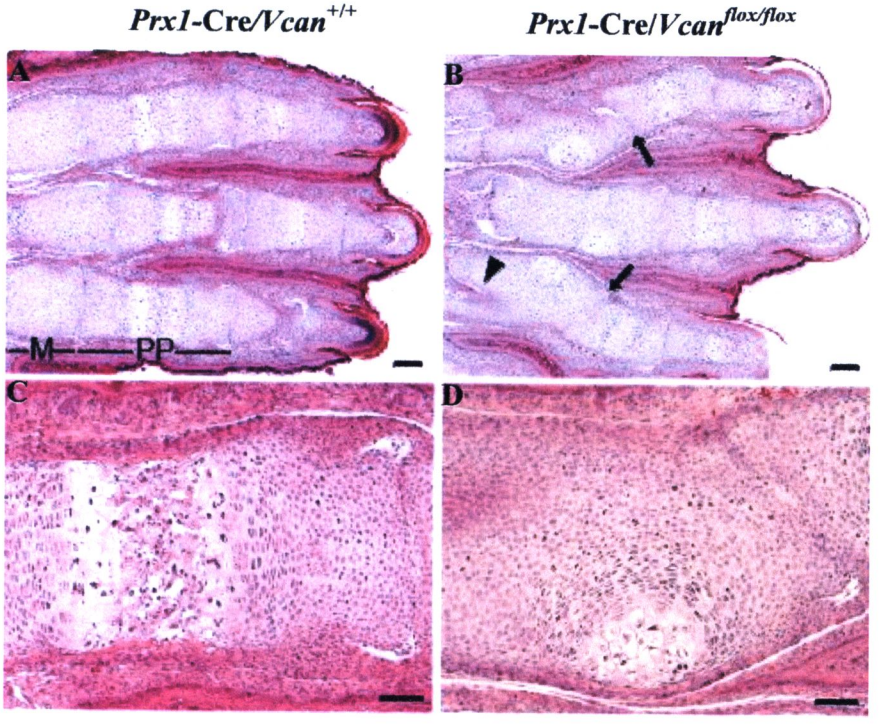

Figure 3.11 Histological analysis of newborn *Prx1*-Cre/*Vcan*$^{+/+}$ (*A* and *C*) and *Prx1*-Cre/*Vcan*$^{flox/flox}$ (*B* and *D*) hind limbs by hematoxylin and eosin (H&E) staining. *Prx1*-Cre/*Vcan*$^{flox/flox}$ digits display joint tilting (*arrows* in *B*) and clefting (*arrowheads* in *B*), formation of hypertrophic chondrocyte nodules in proximal phalanges, and delayed endochondral ossification (*D*). *M*, metatarsus; *PP*, proximal phalanges. *Scale bars*, 200 μm (*A* and *B*) and 40 μm (*C* and *D*). All of the histological sections ($n \geq 5$) of *Prx1*-Cre/*Vcan*$^{flox/flox}$ digits show similar abnormalities.

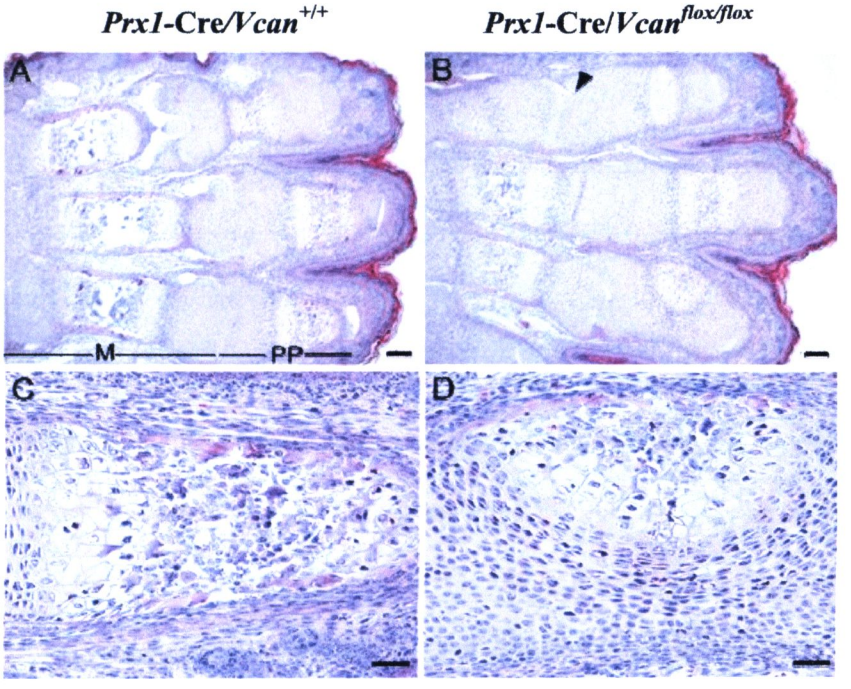

Figure 3.12 Histological analysis of newborn *Prx1*-Cre/*Vcan*$^{+/+}$ (*A* and *C*) and *Prx1*-Cre/*Vcan*$^{flox/flox}$ (*B* and *D*) fore limbs by H&E staining. *Prx1*-Cre/*Vcan*$^{+/+}$ digits display joint tilting (arrowhead in *B*), and formation of hypertrophic chondrocyte nodule in proximal phalanges and delayed endochondral ossification (*D*). M, metacarpus; PP, proximal phalanges. *Scale bars*, 100 μm (*A* and *B*), 25 μm (*C* and *D*).

3.2.3.2 *Prx1*-Cre/*Vcan*$^{flox/flox}$ mice exhibited delayed cartilage development at E15.5, E16.5, and E18.5

To determine the initiation of the deformities, histological analysis on embryonic stages was performed. In staging the embryos, day 0.5 (E0.5) was defined as 12 noon of the day a vaginal plug was found after overnight mating. As shown in figure 3.13, at E18.5, metatarsus of *Prx1*-Cre/*Vcan*$^{+/+}$ showed well organized chondrocyte columns in the growth plate and the primary ossification center with vascular invasion. In contrast, that of *Prx1*-Cre/*Vcan*$^{flox/flox}$ had an aberrant nodule of hypertrophic chondrocytes surrounded by prehypertrophic and proliferative chondrocytes in a concentric pattern (*arrow*), and it had not yet exhibited vascular invasion. At E16.5 and E15.5, metatarsus of *Prx1*-Cre/*Vcan*$^{+/+}$ exhibited a hypertrophic cell mass formation. In contrast, the metatarsus of *Prx1*-Cre/*Vcan*$^{flox/flox}$ contained no hypertrophic chondrocytes yet. At E14.5 and E13.5, the metatarsus of both *Prx1*-Cre/*Vcan*$^{+/+}$ and *Prx1*-Cre/*Vcan*$^{flox/flox}$ contained only a group of differentiating chondrocytes. Although, clefting of some metatarsophalangeal joints was seen at E18.5 but they were obvious in the proximal region of proximal phalanges at E16.5 and E15.5 (*arrow*).

As demonstrated in figure 13.4, at E16.5 and E15.5, *Prx1*-Cre/*Vcan*$^{+/+}$ digits exhibited a horizontally oriented interzone , forming a joint cavity, whereas *Prx1*-Cre/*Vcan*$^{flox/flox}$ digits exhibited a broader interzone of small mesenchymal cells, giving rise to a wedge-shaped or vertical/longitudinal cavity. Concordantly, alcian blue staining of *Prx1*-Cre/*Vcan*$^{+/+}$ hind limb showed well aligned stripes of the interzone, whereas that of *Prx1*-Cre/*Vcan*$^{flox/flox}$ digits revealed tilting of the joint interzone, figure 13.5. When observed at E14.5, the joint interzone, defined as the

area that consists of compact and closely associated mesenchymal cells located along the presumptive joint location (136, 146), did not show a clear joint cavity yet. Hematoxylin and eosin staining exhibited no obvious differences between *Prx1*-Cre/*Vcan*$^{+/+}$ and *Prx1*-Cre/*Vcan*$^{flox/flox}$ in the joint interzone, although there were no clear joint interzone stripes in *Prx1*-Cre/*Vcan*$^{flox/flox}$ compared with *Prx1*-Cre/*Vcan*$^{+/+}$ embryos, figure 13.6.

Taken together, *Prx1*-Cre/*Vcan*$^{flox/flox}$ digits exhibited two abnormalities, delayed chondrocyte differentiation, as observed by a decrease in hypertrophic cells, and tilting of joint surface, which initially appear at E15.5. Formation of hypertrophic chondrocyte nests at E18.5 is probably due to a shift of the columnar axis by tilting of the joint surface.

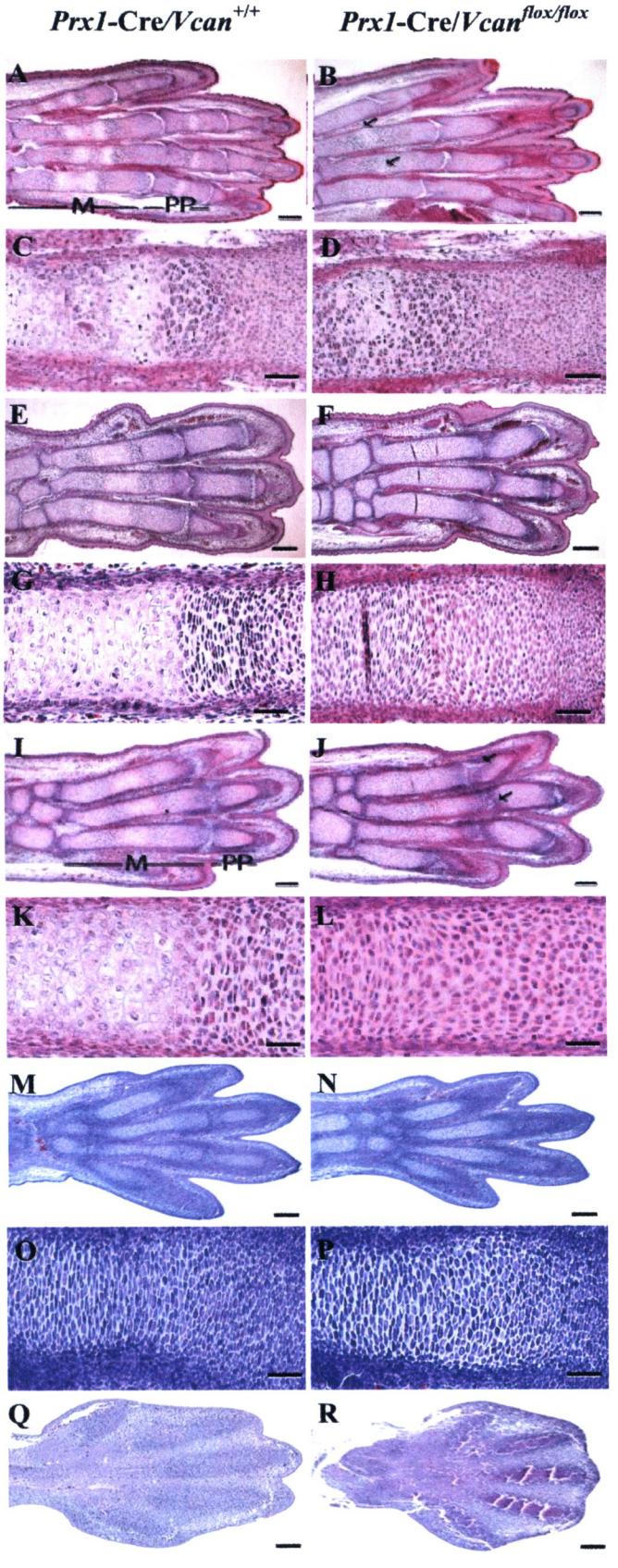
Prx1-Cre/*Vcan*$^{+/+}$
Prx1-Cre/*Vcan*$^{flox/flox}$
A
B
M
PP
C
D
E
F
G
H
I
J
M
PP
K
L
M
N
O
P
Q
R

Figure 3.13 Histological analysis of *Prx1*-Cre/*Vcan*$^{+/+}$ (*A, C, E, G, I, K, M, O* and *Q*) and *Prx1*-Cre/*Vcan*$^{flox/flox}$ (*B, D, F, H, J, L, N* and *P*) hind limbs at various embryonic stages by H&E staining. At E18.5, *Prx1*-Cre/*Vcan*$^{+/+}$ digits (*A* and *C*) demonstrate a well organized columnar structure of prehypertrophic chondrocytes with vascular invasion in metatarsus (*M*) and proximal phalanges (*PP*), whereas *Prx1*-Cre/*Vcan*$^{flox/flox}$ digits (*B* and *D*) exhibit formation of hypertrophic chondrocyte nodules in a concentric pattern in proximal phalanges (*PP*) (*arrows* in *B*) and delayed endochondral ossification of metatarsus (*D*). In addition, clefting of some metatarsophalangeal joints is observed (*B*). At E16.5 (*E, F, G,* and *H*) and E15.5 (*I, J, K,* and *L*), metatarsus of *Prx1*-Cre/*Vcan*$^{+/+}$ (*E, G, I,* and *K*) exhibits prehypertrophic and hypertrophic chondrocyte layers. In contrast, the metatarsus of *Prx1*-Cre/*Vcan*$^{flox/flox}$ (*F, H, J,* and *L*) shows prehypertrophic chondrocytes but not hypertrophic chondrocytes. Moreover, at 15.5, clefting of some metatarsophalangeal joints is clearly observed (*arrows* in *J*). At E14.5 (*M, N, O,* and *P*) and E13.5 (*Q* and *R*), the metatarsus of both *Prx1*-Cre/*Vcan*$^{+/+}$ (*M, O,* and *Q*) and *Prx1*-Cre/*Vcan*$^{flox/flox}$ (*N, P,* and *R*) contains only a group of differentiating chondrocytes. *Scale bars*, 100 μm (*A, B, Q,* and *R*), 40 μm (*C* and *D*), 150 μm (*E, F , I, J, M* and *N*), 50 μm (*G, H, K, L,* O and *P*).

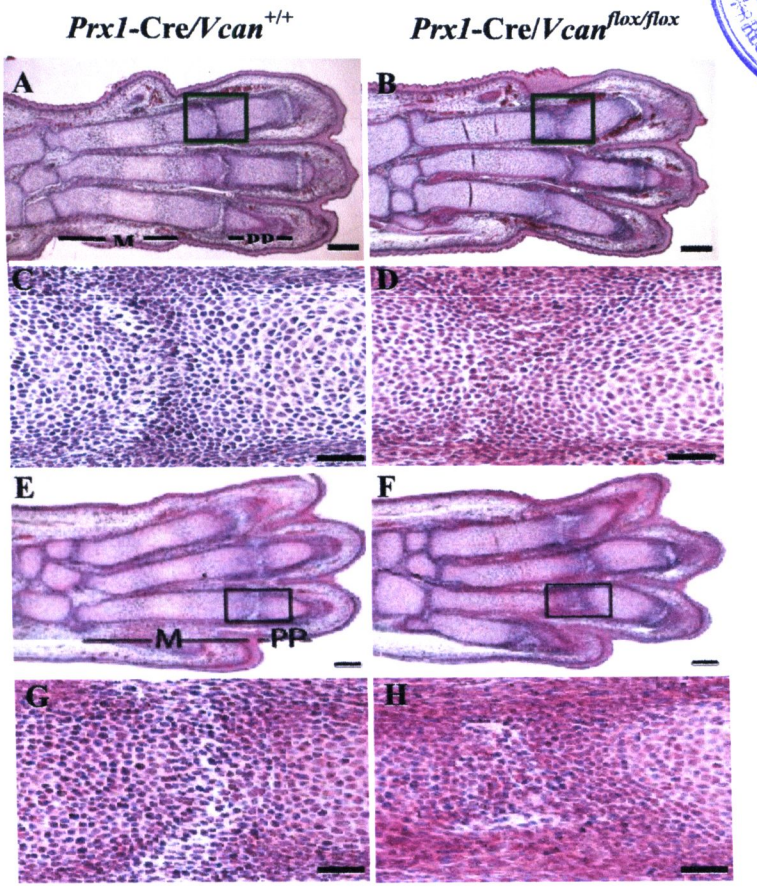

Figure 3.14 Histological analysis of *Prx1*-Cre/*Vcan*$^{+/+}$ (*A, C, E,* and *G*) and *Prx1*-Cre/*Vcan*$^{flox/flox}$ (*B, D, F,* and *H*) hind limbs at E16.5 (*A, B, C,* and *D*) and E15.5 (*E, F, G,* and *H*) by H&E staining. *Prx1*-Cre/*Vcan*$^{+/+}$ digits of both E16.5 (*A* and *C*) and E15.5 (*E* and *F*) display horizontal stripes of the metatarsophalangeal joint interzones (*A* and *C* (as an *enlarged image* of the *boxed area* in *A*)), (*E* and *G* (as an *enlarged image* of the *boxed area* in *E*)). In contrast, *Prx1*-Cre/*Vcan*$^{flox/flox}$ digits display tilted joint interzones (*B* and *D* (as an *enlarged image* of the *boxed area* in *B*)), (*F* and *H* (as an *enlarged image* of the *boxed area* in *F*)). *Scale bars*, 150 μm (*A, B, E* and *F*), 30 μm (*C, D, G* and *H*).

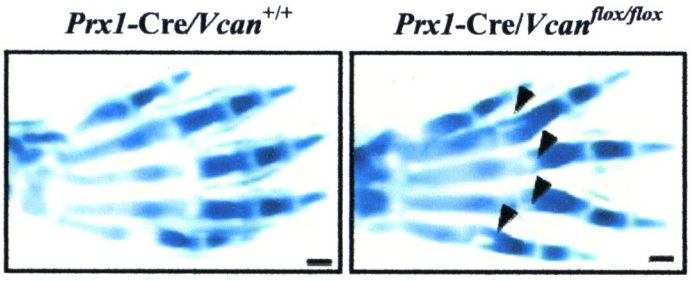

Figure 3.15 Alcian blue staining of *Prx1*-Cre/*Vcan*$^{+/+}$ and *Prx1*-Cre/*Vcan*$^{flox/flox}$ hind limbs at E15.5. *Prx1*-Cre/*Vcan*$^{+/+}$ hind limb shows well aligned stripes of the interzone, whereas that of *Prx1*-Cre/*Vcan*$^{flox/flox}$ digits reveals tilting of the joint interzone (indicated by *arrowheads*).

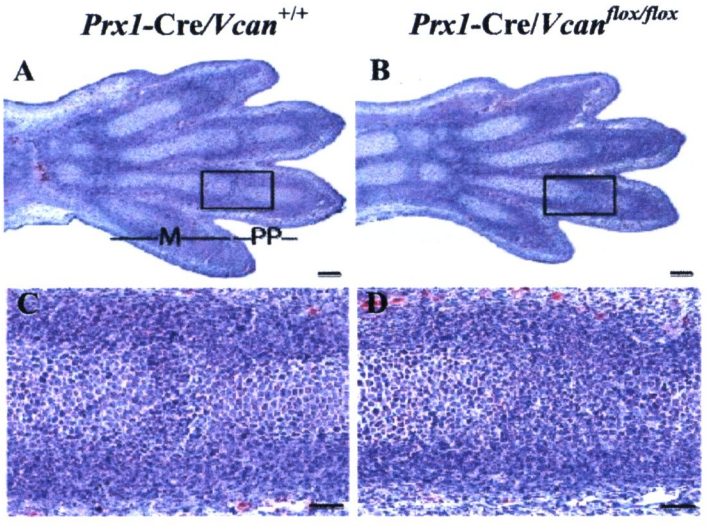

Figure 3.16 Histological analysis of *Prx1*-Cre/*Vcan*$^{+/+}$ and *Prx1*-Cre/*Vcan*$^{flox/flox}$ hind limbs at E14.5 by H&E staining. *Prx1*-Cre/*Vcan*$^{+/+}$ digits display horizontal stripes of the metatarsophalangeal joint interzones (*A*, and *C* as an enlarged image of the boxed area in *A*). Note no obvious differences between *Prx1*-Cre/*Vcan*$^{+/+}$ and *Prx1*-Cre/*Vcan*$^{flox/flox}$ (*B*, and *D* as an enlarged image of the boxed area in *B*) in the joint interzone, although there were no clear joint interzone stripes in *Prx1*-Cre/*Vcan*$^{flox/flox}$, compared with *Prx1*-Cre/*Vcan*$^{+/+}$ embryos. *Scale bars*, 100 μm (*A* and *B*), 30 μm (*C* and *D*).

Since limb shortening found in *Prx1*-Cre/*Vcan*$^{flox/flox}$ digits resulted from the delayed chondrocyte differentiation. To confirm that the shortening did not due to slow proliferation of chondrocytes. Immunostaining for Ki67, a protein expressed in the growing phase, was performed. As demonstrated in figure 13.7, *Prx1*-Cre/*Vcan*$^{+/+}$ and *Prx1*-Cre/*Vcan*$^{flox/flox}$ showed a similar level of proliferation in cartilage.

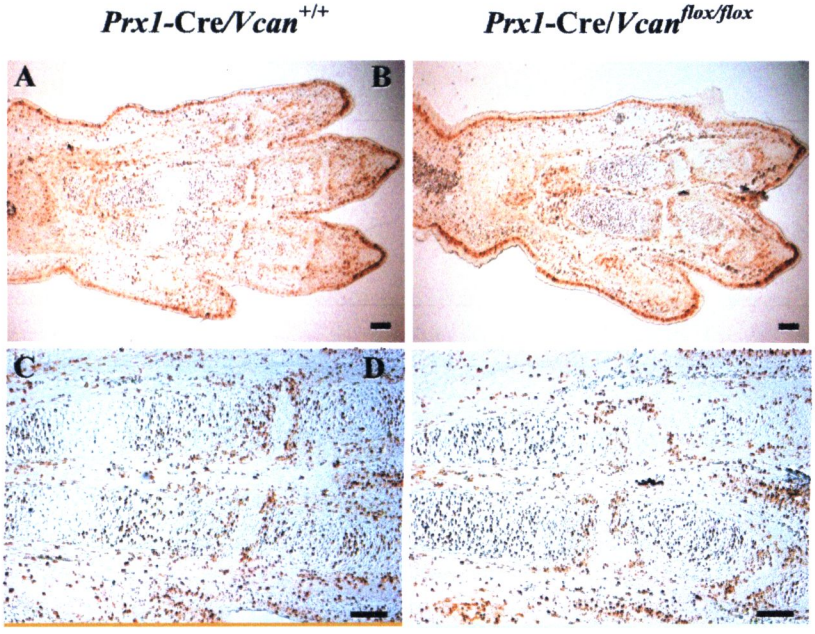

Figure 3.17 Immunostaining for Ki67 of *Prx1*-Cre/*Vcan*$^{+/+}$ (*A* and *C)* and *Prx1*-Cre/*Vcan*$^{flox/flox}$ (*B* and *D)* hind limbs at E15.5. The nuclei positive for Ki67 staining in cartilage is similar between *Prx1*-Cre/*Vcan*$^{+/+}$ and *Prx1*-Cre/*Vcan*$^{flox/flox}$. *Scale bars*, 100 μm (*A* and *B*), 50 μm (*C* and *D*).

3.3 Versican distribution in mice digits

3.3.1 Versican is absent in *Prx1*-Cre/*Vcan*$^{flox/flox}$ digits

As the deformities found in hind limbs supposed to be resulted from the loss of versican, therefore, the expression patterns of versican may be altered. Next, the expression patterns of versican at newborn, E16.5, E15.5, and E13.5 were examined. Immunostaining was shown in figure 3.18, whereas versican was strongly immunostained in the joint interzone and perichondrium, and moderately immunostained in the proliferative zone of cartilage in *Prx1*-Cre/*Vcan*$^{+/+}$ hind limbs of newborn, E16.5, and E15.5, it was not immunostained in the interzone, perichondrium, and cartilage of *Prx1*-Cre/*Vcan*$^{flox/flox}$ hind limbs. At E13.5, versican was immunostained in the digital stripes and moderately immonostained in the interdigital areas in *Prx1*-Cre/*Vcan*$^{+/+}$ hind limbs. In contrast, it was not immunostained in *Prx1*-Cre/*Vcan*$^{flox/flox}$ hind limbs. According to the previous results, the abnormalities were initiated at E15.5. Therefore, hind limbs at E15.5 were used for in-depth investigation.

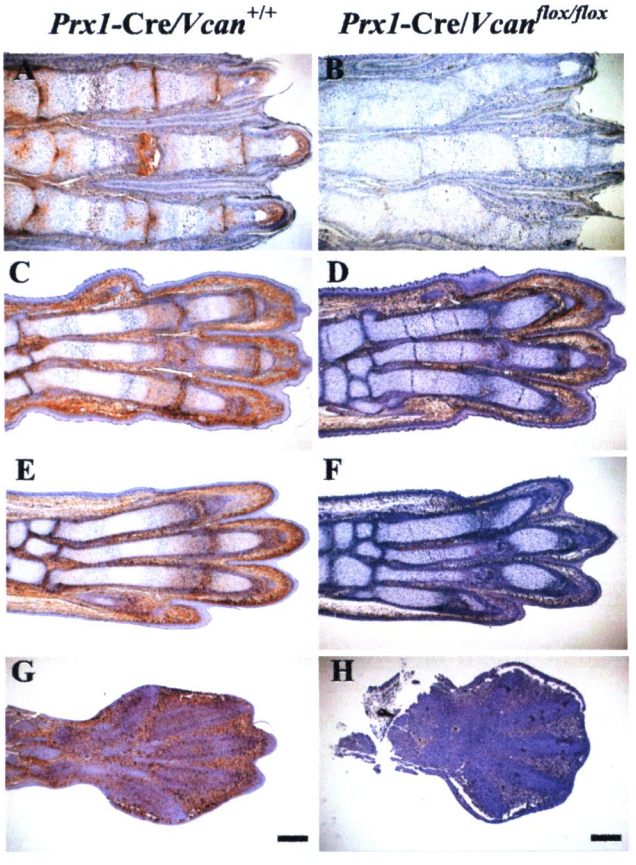

Figure 3.18 Immunostaining for versican of *Prx1*-Cre/*Vcan*$^{+/+}$ and *Prx1*-Cre/*Vcan*$^{flox/flox}$ hind limbs at newborn (*A* and *B*), E16.5 (*C* and *D*), E15.5 (*E* and *F*), and E13.5 (*G* and *H*) is shown. In *Prx1*-Cre/*Vcan*$^{+/+}$ digits (*A, C* and *E*), versican is strongly immunostained in the interzone and perichondrium and moderately immunostained in the proliferative zone of cartilage, whereas in *Prx1*-Cre/*Vcan*$^{flox/flox}$ digits (*B, D* and *F*), versican is immunostained neither in the interzone, the perichondrium, nor the proliferative zone of cartilage. At E13.5, in *Prx1*-Cre/*Vcan*$^{+/+}$ digits (*G*), versican is immunostained in the digital stripes and interdigital areas, whereas in *Prx1*-Cre/*Vcan*$^{flox/flox}$ digits (*H*), versican is not either immunostained. *Scale bars*, 120 μm.

3.3.2 Cre immunostaining and β-galactosidase activity supported the lack of versican expression in *Prx1*-Cre/*Vcan*$^{flox/flox}$ digits

Immunostaining for versican of E15.5 hind limbs was displayed in figure 3.19. Versican was strongly immunostained in the joint interzone and perichondrium and moderately immunostained in the proliferative zone of cartilage in *Prx1*-Cre/*Vcan*$^{+/+}$, whereas it was not immunostained in the interzone, perichondrium, and cartilage of *Prx1*-Cre/*Vcan*$^{flox/flox}$. The regions lacking versican specifically in *Prx1*-Cre/*Vcan*$^{flox/flox}$ were supposed to be the regions where Cre enzyme was or had been expressed. When immunostained, Cre enzyme was observed in the perichondrium and the interzone in *Prx1*-Cre/*Vcan*$^{flox/flox}$, as shown in figure 3.20. Furthermore, to confirm the lack of versican, *Prx1*-Cre activity was analyzed by ROSA26 reporter mice as explained in material and methods. By X-gal staining at E14.5 of *Prx1*-Cre/R26R, β-galactosidase activity was found in chondrocytes as well as in perichondrium, figure 3.21. These observations support the lack of versican expression in *Prx1*-Cre/*Vcan*$^{flox/flox}$.

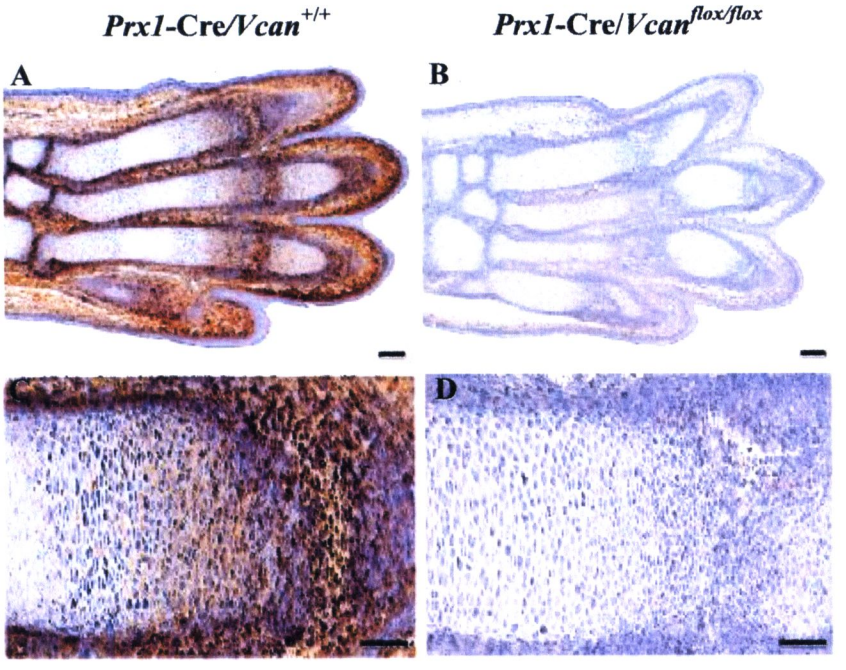

Figure 3.19 Immunostaining for versican of *Prx1*-Cre/*Vcan*$^{+/+}$ (*A* and *C)* and *Prx1*-Cre/*Vcan*$^{flox/flox}$ (*B* and *D)* hind limbs at E15.5. *Scale bars*, 120 μm (*A* and *B*), 70 μm (*C* and *D*).

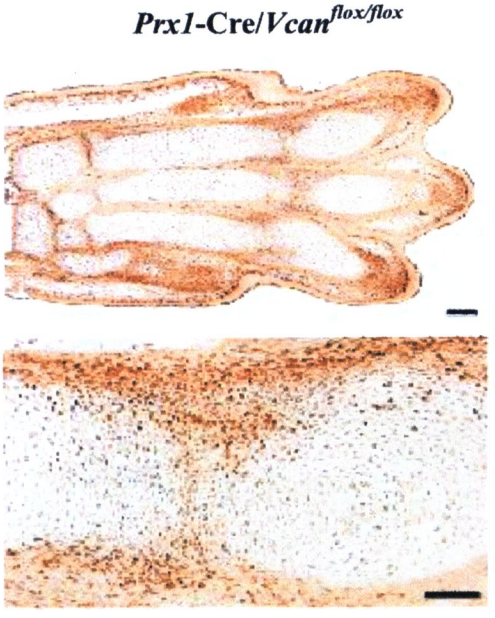

Figure 3.20 Immunostaining for Cre enzyme of E15.5 *Prx1*-Cre/*Vcan*$^{flox/flox}$ hind limbs at low (*top*) and high (*bottom*) magnifications. Cre enzyme is immunostained in the perichondrium and in the tilted interzone. *Scale bars*, 100 μm and 50 μm, respectively. Two individual *Prx1*-Cre/*Vcan*$^{flox/flox}$ digits showed the same abnormalities.

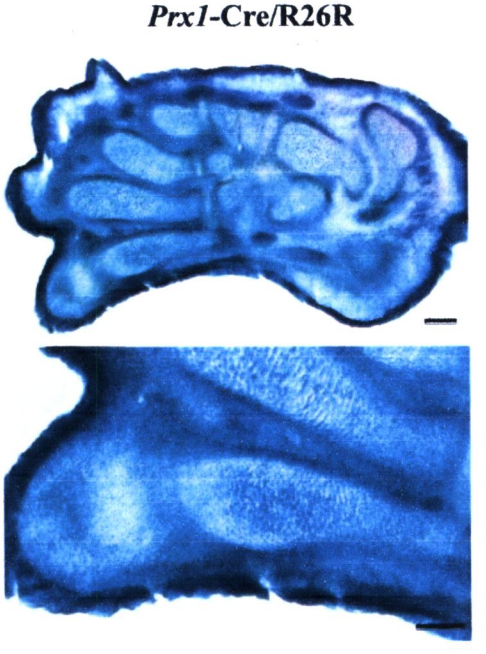

Figure 3.21 β-galactosidase staining of hindlimbs at E14.5 at low (*top*) and high (*bottom*) magnifications. β-gal activity is found in chondrocytes and in perichondrium. *Scale bars*, 100 μm and 80 μm, respectively.

3.4 Distribution of hyaluronan and its binding molecules in the joint interzone

Versican is known to bind with HA through G1 domain, and HA itself can also binds to other ECM molecules. Thus, the absence of versican supposed to affect their distributions. To gain insight into the mechanism how the absence of versican affected the distribution of those molecules that led to joint deformity, then HA and its binding molecules were examined by immunofluorescent staining.

Whereas HA is bound to both aggrecan and link protein and profoundly incorporated as the proteoglycan aggregate in cartilage, it is also accumulated in the joint interzone, which contributes to joint formation. Recent studies suggested that the accumulated HA mediates signals via CD44 toward joint cavity formation (237). Because the immunostaining, figure 3.22, demonstrated the presence of versican in the interzone at E15.5 of *Prx1*-Cre/*Vcan*$^{+/+}$ and its absence in *Prx1*-Cre/*Vcan*$^{flox/flox}$, therefore versican is speculated to be necessary for adequate levels of HA accumulation and HA-mediated signaling toward joint formation, and that its absence caused the joint abnormality.

As demonstrated in figure 3.22, by the detection method using biotinylated HABP, accumulation of HA was observed at a similar level in the interzone of both *Prx1*-Cre/*Vcan*$^{+/+}$ and *Prx1*-Cre/*Vcan*$^{flox/flox}$. Immunofluorescent staining displayed the presence of versican in the interzone, future articular surface, and perichondrium in *Prx1*-Cre/*Vcan*$^{+/+}$ and its absence in *Prx1*-Cre/*Vcan*$^{flox/flox}$. Immunofluorescent staining for aggrecan that clearly demarcates cartilage tissue from the interzone revealed clefting of the future joint surface in *Prx1*-Cre/*Vcan*$^{flox/flox}$. Whereas link protein was colocalized with aggrecan in *Prx1*-Cre/*Vcan*$^{+/+}$, it was also present in the interzone in *Prx1*-Cre/*Vcan*$^{flox/flox}$. These observations suggest that whereas versican

retains HA in the interzone, link protein does so in the absence of versican. CD44 was not detected at E15.5, eliminating involvement of CD44 in the joint formation at this embryonic stage. In addition, the expression of CD44 in the joint was not detected until E18.5, figure 3.23.

There is an evidence to suggest that extracellular-signal-related kinases (ERK1/2) are important in the mechanotransduction pathway (197, 198), and phosphorylated ERK1/2 has been found to be presented at the sites of joint cavitation and is also preserved after cavitation (197, 199). Also, the Wnt/β-catenin canonical signaling pathway has been reported to be necessary and sufficient for the induction of synovial joints in the limb (148). Hence, to test whether these two pathways are altered during joint formation, the immunostaining for phosphorylated ERK1/2 and β-catenin was performed. By immunostaining of the joint interzone at E15.5, phosphorylated ERK1/2 was immunostained at the joint interzone in both *Prx1*-Cre/*Vcan*$^{+/+}$ and *Prx1*-Cre/*Vcan*$^{flox/flox}$, figure 3.24. As shown in figure 3.24, β-catenin was expressed in closely associated mesenchymal cells at similar levels between *Prx1*-Cre/*Vcan*$^{+/+}$ and *Prx1*-Cre/*Vcan*$^{flox/flox}$ at the joint interzone.

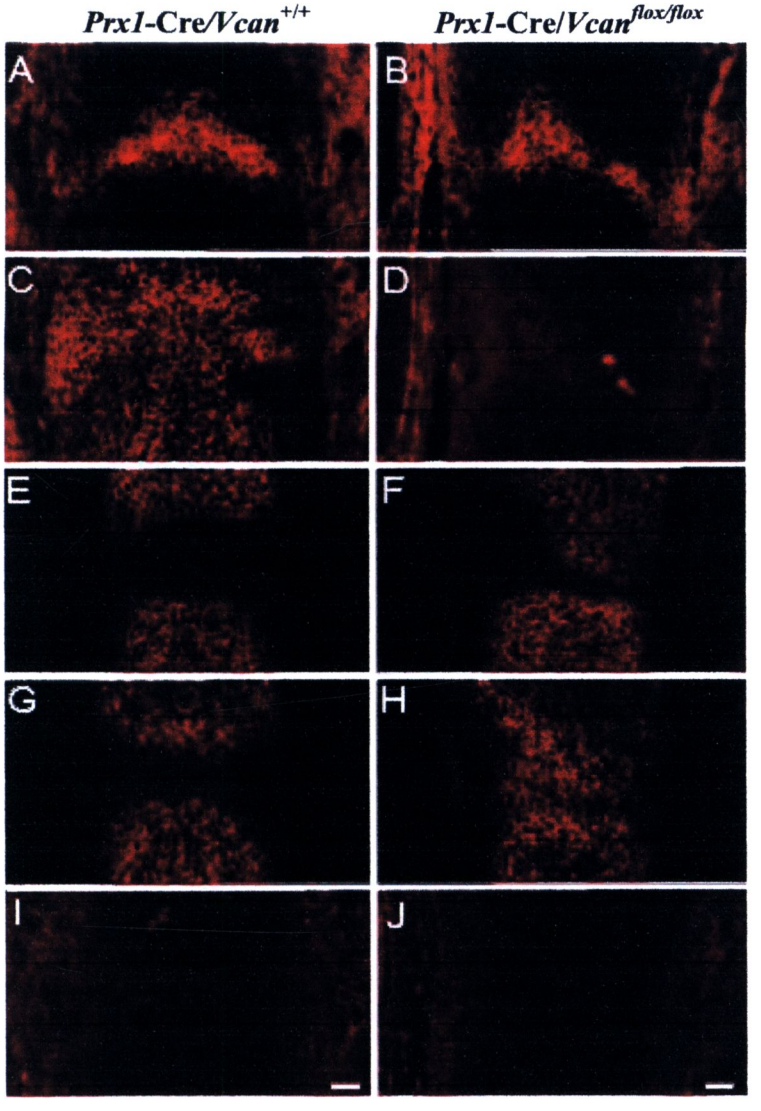

Figure 3.22 Distributions of HA and HA-binding molecules in the metatarsophalangeal joint interzone at E15.5 of *Prx1*-Cre/*Vcan*$^{+/+}$ (*A*, *C*, *E*, *G*, and *I*) and *Prx1*-Cre/*Vcan*$^{flox/flox}$ (*B*, *D*, *F*, *H*, and *J*). By detection of HA using b-HABP, unincorporated HA is accumulated at a similar level in the joint interzone of both *Prx1*-Cre/*Vcan*$^{+/+}$ and *Prx1*-Cre/*Vcan*$^{flox/flox}$ (*A* and *B*). Immunofluorescent staining confirms the presence of versican in the interzone, future articular surface, and perichondrium in *Prx1*-Cre/*Vcan*$^{+/+}$ and its absence in *Prx1*-Cre/*Vcan*$^{flox/flox}$ (*C* and *D*).

Immunofluorescent staining for aggrecan, demarcating the cartilage tissue, demonstrates tilting of the joint surface in *Prx1*-Cre/*Vcan*$^{flox/flox}$ (*E* and *F*). Link protein (*LP*) is immunostained in cartilage of *Prx1*-Cre/*Vcan*$^{+/+}$ (*G*), whereas it is immunostained in both cartilage and the joint interzone of *Prx1*-Cre/*Vcan*$^{flox/flox}$ (*H*). CD44 is not detected in both *Prx1*-Cre/*Vcan*$^{+/+}$ and *Prx1*-Cre/*Vcan*$^{flox/flox}$ at this stage (*I*, *J*), eliminating the possibility of its participation in joint cavitation. *Scale bars*, 30 μm. Immunostaining was performed on at least two individual digits for *Prx1*-Cre/*Vcan*$^{+/+}$ and *Prx1*-Cre/*Vcan*$^{flox/flox}$, with the same immunostaining patterns.

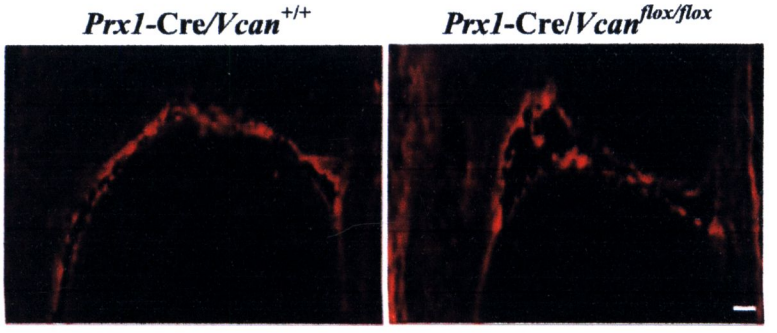

Figure 3.23 Immunofluorescent staining for CD44 of *Prx1*-Cre/*Vcan*$^{+/+}$ and *Prx1*-Cre/*Vcan*$^{flox/flox}$ metatarsophalangeal joint at E18.5. *Scale bars*, 40 μm.

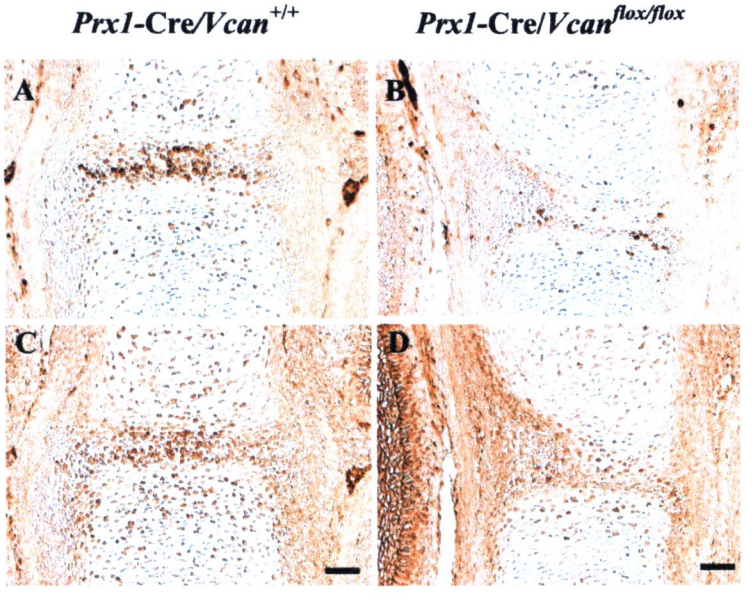

Figure 3.24 Immunostaining for pERK1/2 (*A* and *B*) and β-catenin (*C* and *D*) of *Prx1*-Cre/*Vcan*$^{+/+}$ (*A* and *C*) and *Prx1*-Cre/*Vcan*$^{flox/flox}$ (*B* and *D*) metatarsophalangeal joint at E15.5. *Scale bars*, 40 μm.

3.5 TGF-β signaling is attenuated in *Prx1*-Cre/*Vcan*$^{flox/flox}$ interzone

When compared with animals that exhibit joint malformation, the abnormalities found in *Prx1*-Cre/*Vcan*$^{flox/flox}$ embryos resembled conditional knock-out mice of TβRII generated by crossing *Prx1*-Cre transgenic and *Tgfbr2*$^{flox/flox}$ mice, which exhibit the failure of joint interzone development (167). Therefore, TGF-β signaling was speculated to be altered in *Prx1*-Cre/*Vcan*$^{flox/flox}$. When the expression patterns of TGF-β and its related molecules were investigated by immunostaining as displayed in figure 3.25, whereas TGF-β was localized in *Prx1*-Cre/*Vcan*$^{+/+}$ interzone, it was not detected in *Prx1*-Cre/*Vcan*$^{flox/flox}$. TβRII was broadly immunostained in interzone, perichondrium, and chondrocytes of both *Prx1*-Cre/*Vcan*$^{+/+}$ and *Prx1*-Cre/*Vcan*$^{flox/flox}$ digits. Phospho-Smad2/3 was detected in the nuclei of cells in the *Prx1*-Cre/*Vcan*$^{+/+}$ interzone. In contrast, it was not detected in *Prx1*-Cre/*Vcan*$^{flox/flox}$. These results indicate that TGF-β signaling is substantially diminished in *Prx1*-Cre/*Vcan*$^{flox/flox}$, although the expression of its receptor is unaffected.

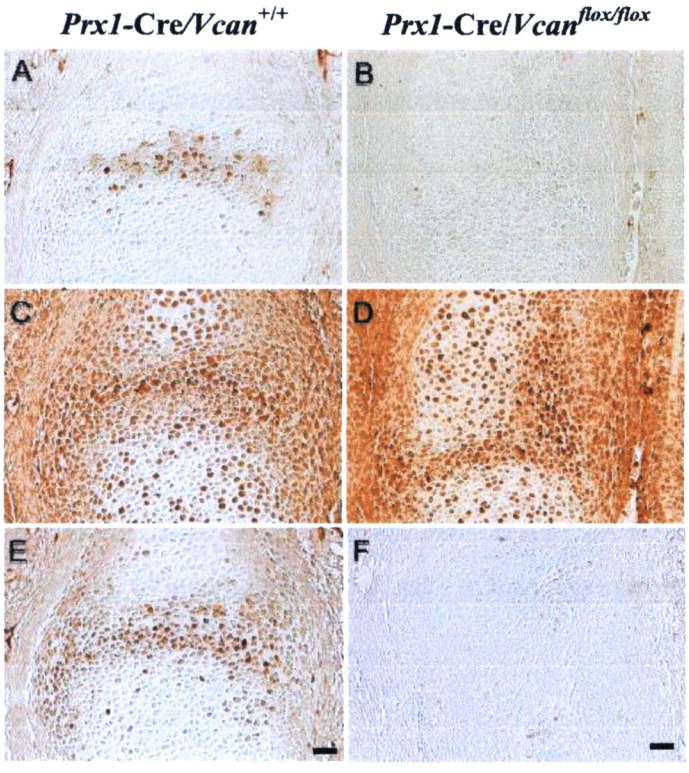

Figure 3.25 Immunostaining patterns of TGF-β (*A* and *B*), TβRII (*C* and *D*), and phospho-Smad2/3 (*E* and *F*) in the metatarsophalangeal joint interzone at E15.5 of *Prx1*-Cre/*Vcan*$^{+/+}$ (*A*, *C*, and *E*) and *Prx1*-Cre/*Vcan*$^{flox/flox}$ (*B*, *D*, and *F*). Whereas TGF-β is localized in the *Prx1*-Cre/*Vcan*$^{+/+}$ joint interzone (*A*), it is not detected in *Prx1*-Cre/*Vcan*$^{flox/flox}$ (*B*). TβRII is broadly immunostained in the joint interzone, perichondrium, and chondrocytes of both *Prx1*-Cre/*Vcan*$^{+/+}$ (*C*) and *Prx1*-Cre/*Vcan*$^{flox/flox}$ (*D*). Whereas phospho-Smad2/3 is found in the nuclei of cells in the *Prx1*-Cre/*Vcan*$^{+/+}$ interzone, it is not detected in *Prx1*-Cre/*Vcan*$^{flox/flox}$. *Scale bars*, 20μm. Immunostaining was performed on at least two individual digits for *Prx1*-Cre/*Vcan*$^{+/+}$ and *Prx1*-Cre/*Vcan*$^{flox/flox}$, with the same immunostaining patterns.

3.6 Impaired mesenchymal condensations in *Prx1*-Cre/*Vcan*$^{flox/flox}$ lead to delayed chondrocyte differentiation in micromass culture

Prx1-Cre/*Vcan*$^{flox/flox}$ digits showed a delay in chondrocyte differentiation at E15.5 (figure 3.14). Interestingly, whole mount alcian blue staining in figure 3.26 demonstrated a decrease in areas positive for alcian blue in *Prx1*-Cre/*Vcan*$^{flox/flox}$ hind limbs compared with *Prx1*-Cre/*Vcan*$^{+/+}$, suggesting that delay of chondrocyte differentiation took place prior to E13.5. To obtain insight into the mechanisms of delayed chondrocyte differentiation in *Prx1*-Cre/*Vcan*$^{flox/flox}$ digits, limb bud mesenchymal cells were investigated by a high density micromass culture system.

3.6.1 β-galactosidase activity supports the lack of versican expression in micromass culture

Since versican will be excised by *Prx1*-Cre activity, the successfully abrogated versican expression in all of the mesenchymal cells in the micromass was confirmed by X-gal staining. Cells positive for X-gal staining of micromass obtained from *Prx1*-Cre/R26R limb buds was shown in figure 3.27.

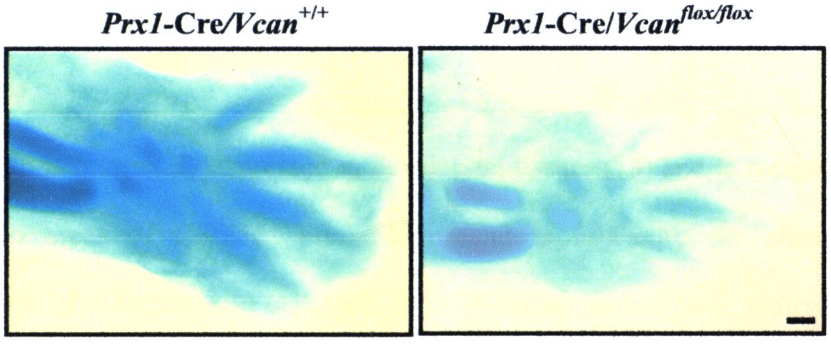

Figure 3.26 Alcian blue staining of hind limbs at E13.5. Patterns of both *Prx1*-Cre/*Vcan*$^{+/+}$ and *Prx1*-Cre/*Vcan*$^{flox/flox}$. *Scale bars*, 100μm.

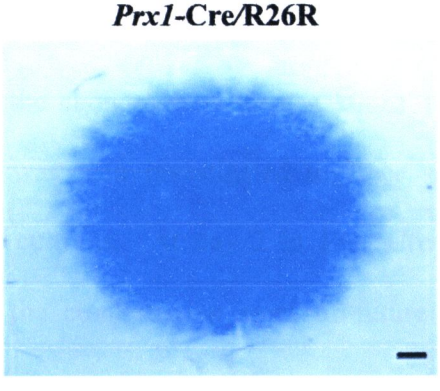

Figure 3.27 A pattern stained for β-galactosidase of *Prx1*-Cre/R26R micromass culture. *Scale Bar*, 120 μm.

3.6.2 Versican expression patterns in micromass culture at day 3, day 6, and day 9

Versican is transiently expressed in developing tissues (13) and in mesenchymal condensation areas of cartilage primordium, and is necessary for chondrocyte differentiation of mesenchymal cells (16, 17). Previous studied have indicated that versican is transiently expressed at high levels and rapidly diminished during cartilage development (6, 14). Thus, the decrease of versican expression and the increase of chondrogenic differentiation marker such as aggrecan, is somehow overlapped during chondrocyte development. Therefore, to appropriately observed chondrocyte differentiation, timing of micromass cultures from *Prx1*-Cre/*Vcan*$^{+/+}$ was optimized.

Prior to condensations, the prechondrogenic mesenchymal cells express cell surface molecules that bind PNA and allow condensations to be visualised (100, 101, 102). In order to confirm the chondrogenic condensations, the expression of PNA specific binding molecule was then investigated together with the expression of versican in the micromass cultures. At day 3 in *Prx1*-Cre/*Vcan*$^{+/+}$, versican was localized in the center of the condensation areas of future cartilaginous nodules, confirming its transient high expression in mesenchymal condensation areas. At day 6 and day 9, it was found in areas surrounding the cartilaginous nodules, designated perinodular regions, figure 3.28 and 29. As shown in figure 3.28 and 29, the present of PNA at day 3, day 6, and day 9 was similarly localized that of versican expression patterns, supporting the chondrogenic condensations. Taken together, micromass culture at day 6 was suitable for investigation of the mechanism underlying chondrogenic differentiation.

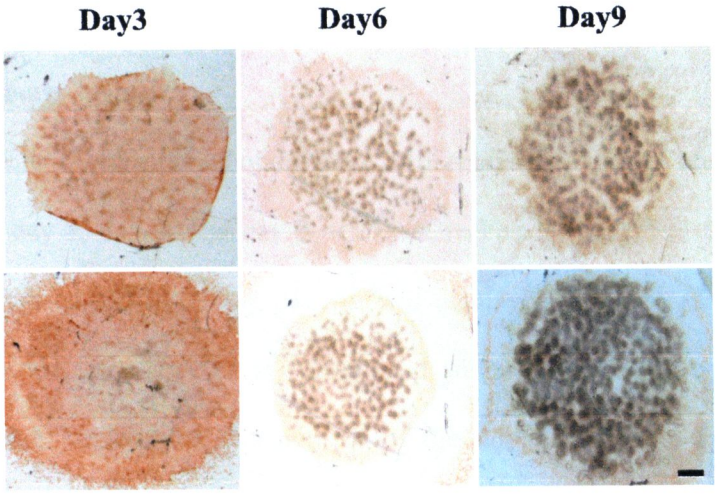

Figure 3.28 Patterns of staining for versican and PNA in *Prx1*-Cre/*Vcan*$^{+/+}$ micromass cultures at day 3, day 6, and day 9. *Scale bars*, 100μm.

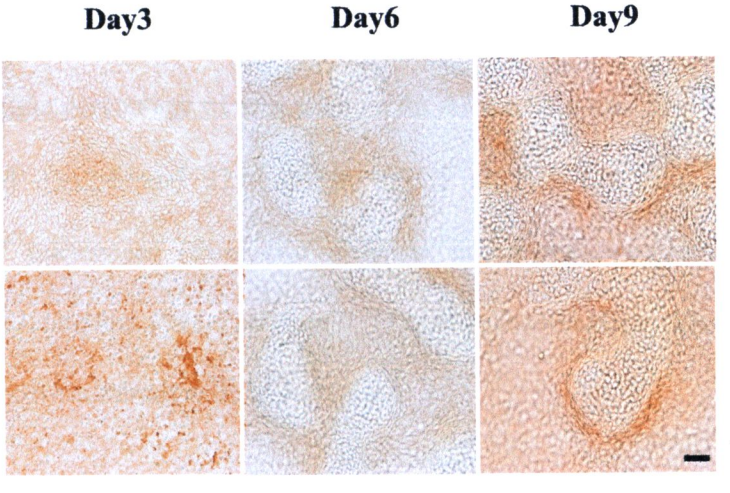

Figure 3.29 Patterns of staining for versican and PNA in *Prx1*-Cre/*Vcan*$^{+/+}$ micromass cultures at day 3, day 6, and day 9. *Scale bars*, 40 μm.

3.6.3 *Prx1*-Cre/*Vcan*$^{flox/flox}$ exhibits delayed chondrocyte differentiation in micromass culture

In addition, to observe chondrogenic differentiation, alcian blue staining of micromass at day 3, day 6, and day 9 of *Prx1*-Cre/*Vcan*$^{+/+}$ and *Prx1*-Cre/*Vcan*$^{flox/flox}$ was then performed. The staining patterns was displayed in figure 3.30, at day 3 of micromass culture, *Prx1*-Cre/*Vcan*$^{+/+}$ contained some cartilaginous nodules stained with alcian blue. At day 6, the number of the nodules positive for alcian blue increased considerably. At day 9, their number further increased, and the nodules in the center were strongly stained with Alcian blue. When compared with *Prx1*-Cre/*Vcan*$^{+/+}$, *Prx1*-Cre/*Vcan*$^{flox/flox}$ micromass at day 3 contained a small number of cartilaginous nodules. At day 6, the number of the nodules positive for alcian blue increased, but it remained smaller than *Prx1*-Cre/*Vcan*$^{+/+}$. At day 9, their number increased, but the nodules remained smaller than *Prx1*-Cre/*Vcan*$^{+/+}$ micromass. Quantitatively, the percentage of area positive for Alcian blue was 21±2 and 18±4.2% at day 3, and 35±2.6 and 32±5.6% at day 6 in *Prx1*-Cre/*Vcan*$^{+/+}$ and *Prx1*-Cre/*Vcan*$^{flox/flox}$ micromass (from two different littermates), respectively. These observations indicate that *Prx1*-Cre/*Vcan*$^{flox/flox}$ cells in the mesenchymal condensation showed a delay in chondrocyte differentiation.

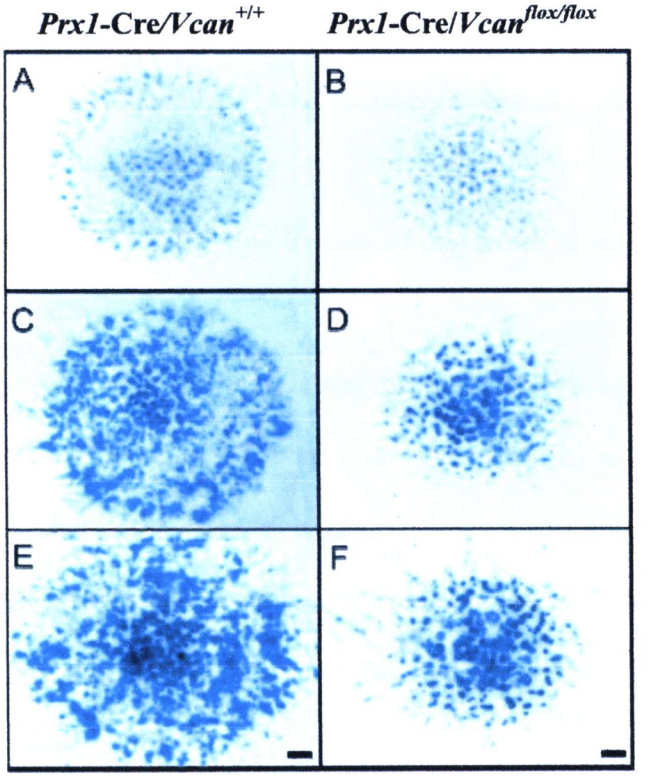

Figure 3.30 Patterns of micromass stained by alcian blue at day 3 (*A* and *B*), 6 (*C* and *D*), and 9 (*E* and *F*) of *Prx1*-Cre/*Vcan*$^{+/+}$ (*A*, *C*, and *E*) and *Prx1*-Cre/*Vcan*$^{flox/flox}$ (*B*, *D*, and *F*). At day 3, micromass of *Prx1*-Cre/*Vcan*$^{+/+}$ contains some cartilaginous nodules stained with alcian blue (*A*), whereas that of *Prx1*-Cre/*Vcan*$^{flox/flox}$ contains a smaller number of them (*B*). At day 6, the number of the nodules positive for alcian blue in micromass of *Prx1*-Cre/*Vcan*$^{flox/flox}$ increases, but it remains smaller than that of *Prx1*-Cre/*Vcan*$^{+/+}$ (*C* and *D*). At day 9, the number of cartilaginous nodules in micromass of *Prx1*-Cre/*Vcan*$^{+/+}$ further increases, and the nodules in the center become strongly stained with alcian blue (*E*). Although the number of cartilaginous nodules in micromass of *Prx1*-Cre/*Vcan*$^{flox/flox}$ increases during culture (*F*), it remains smaller than *Prx1*-Cre/*Vcan*$^{+/+}$. *Scale bars*, 300 μm.

3.7 Impaired mesenchymal condensations and altered TGF-β signaling in the micromass of *Prx1*-Cre/*Vcan*$^{flox/flox}$ lead to delayed chondrocyte differentiation

3.7.1 Expression patterns of TGF-β and its related molecules in micromass culture at day 3, day 6

TGF-β signaling is known to facilitate chondrocyte differentiation because the chondrocyte differentiation medium of bone marrow mesenchymal stem cells contains TGF-β (238). Hence, the expression of TGF-β and its related molecules as well as versican expression was further examined from micromass cultures of *Prx1*-Cre/*Vcan*$^{+/+}$. As demonstrated in figure 3.31, at day 3, TGF-β was mostly localized in the center of the condensation areas of the cartilaginous nodules, TβRII was found in the center and the internodular regions, pSmad2/3 was found in the center areas of the cartilaginous nodules. At day 6 of culture, TGF-β was localized in the center of the nodules, however, it also shifted to the perinodular regions, TβRII was found in the center and the internodular regions, and pSmad2/3 was found in the center and in the perinodular areas of the cartilagenous nodules, figure 3.32. Interestingly, when compared, the staining patterns in micromass cultures of versican and TGF-β were resemble, figure 3.33.

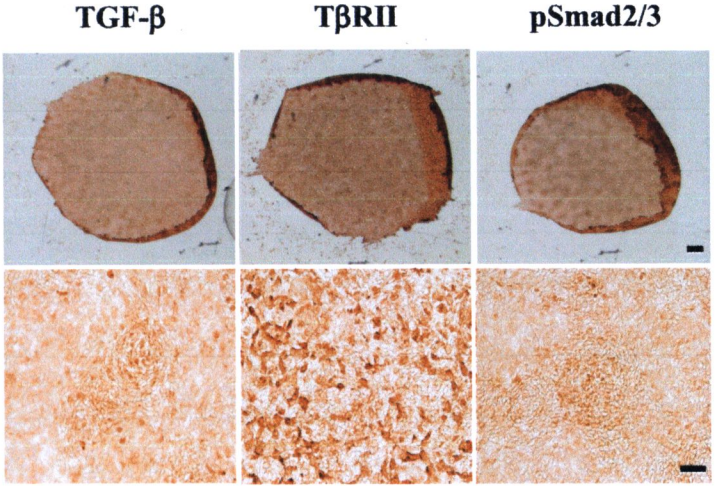

Figure 3.31 Patterns of immunostaining for TGF-β, TβRII, and pSmad2/3 in *Prx1*-Cre/*Vcan*$^{+/+}$ micromass cultures at day 3. *Scale bars*, 100 μm (*top*), 40 μm (*bottom*).

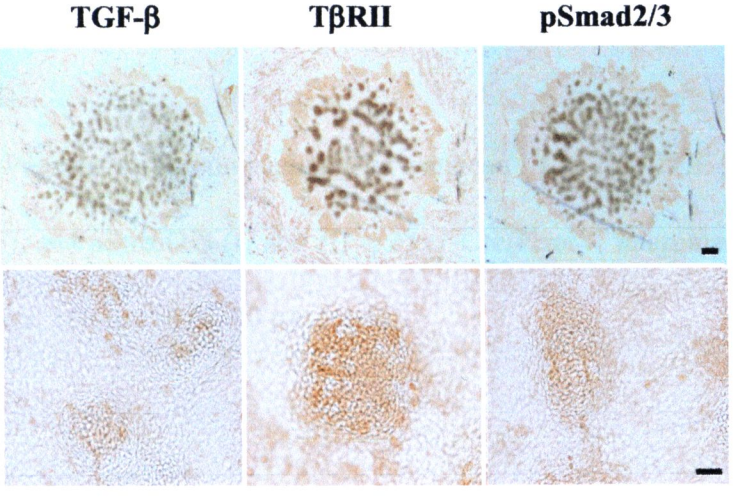

Figure 3.32 Patterns of immunostaining for TGF-β, TβRII, and pSmad2/3 in *Prx1*-Cre/*Vcan*$^{+/+}$ micromass cultures at day 6. *Scale bars*, 100 μm (*top*), 40 μm (*bottom*).

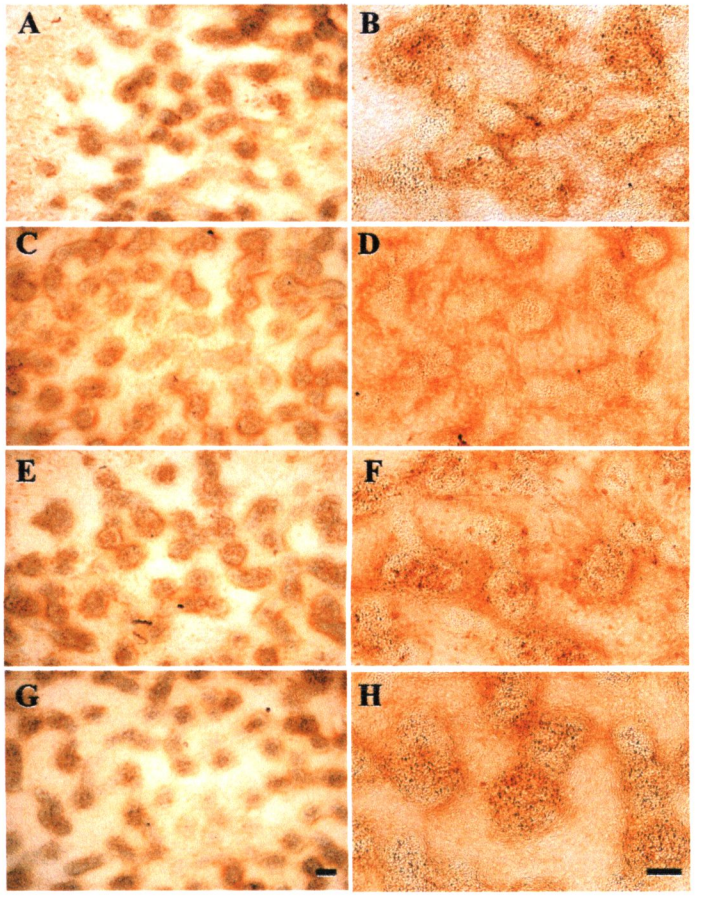

Figure 3.33 Patterns of immunostaining for versican (*A* and *B*) TGF-β (*C* and *D*), TβRII (*E* and *F*), and pSmad2/3 (*G* and *H*) in *Prx1*-Cre/*Vcan*$^{+/+}$ micromass cultures at day 6. *Scale bars*, 100 μm (*left*), 40 μm (*right*).

3.7.2 TGF-β signaling is altered in the micromass of *Prx1*-Cre/*Vcan*$^{flox/flox}$

Due to the conditional removal of versican, TGF-β localization was assumed to be altered. As shown in figure 3.25, TGF-β was substantially decreased in the *Prx1*-Cre/*Vcan*$^{flox/flox}$ interzone at E15.5. TGF-β signaling was speculated to be similarly down-regulated in *Prx1*-Cre/*Vcan*$^{flox/flox}$ micromass culture, which caused the delay in chondrocyte differentiation. By immunofluorescent staining demonstrated in figure 3.34, TGF-β was localized in the perinodular regions in *Prx1*-Cre/*Vcan*$^{+/+}$ micromass, similar to versican. In contrast, it was observed diffusely in the extracellular matrix at a substantially lower intensity in *Prx1*-Cre/*Vcan*$^{flox/flox}$ micromass. When merged, both versican and TGF-β were well co-localized in *Prx1*-Cre/*Vcan*$^{+/+}$ micromass. TβRII was immunostained mainly in the perinodular regions in both *Prx1*-Cre/*Vcan*$^{+/+}$ and *Prx1*-Cre/*Vcan*$^{flox/flox}$ micromass. In addition, it was immunostained rather diffusely in *Prx1*-Cre/*Vcan*$^{flox/flox}$. Phospho-Smad2/3 was immunostained strongly in the nuclei of perinodular cells and moderately in the nuclei of chondrocytes within the nodules in the *Prx1*-Cre/*Vcan*$^{+/+}$ micromass. In contrast, it was immunostained in the nuclei of chondrocytes in the nodules moderately and in those of the cells weakly in the perinodular regions of the *Prx1*-Cre/*Vcan*$^{flox/flox}$ micromass. These results strongly suggest that versican accumulates TGF-β in the extracellular matrix of the perinodular regions and facilitates its signaling. The diffuse patterns of TGF-β in the extracellular matrix and the positive immunostaining for phospho-Smad2/3 in chondrocytes indicate that TGF-β signaling functions toward the differentiation even in the absence of versican. By Western blot analysis, *Prx1*-Cre/*Vcan*$^{flox/flox}$ micromass exhibited comparable expression levels of TGF-β, figure 3.35.

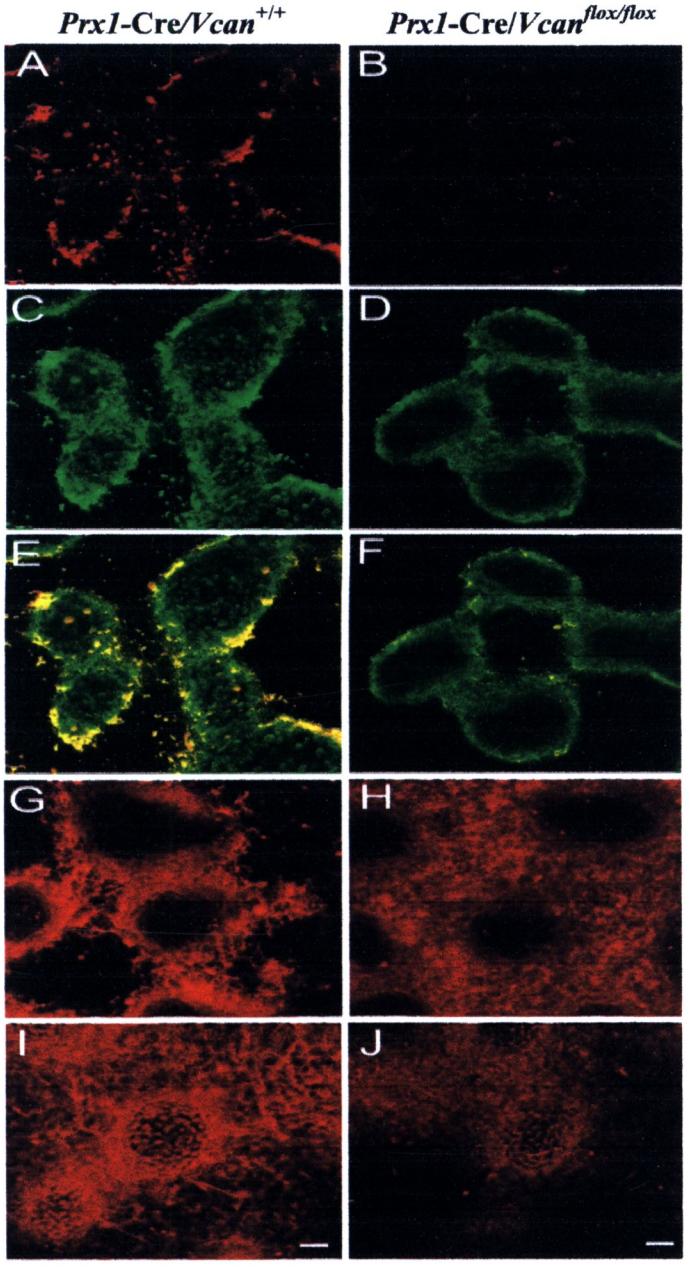

Figure 3.34 Immunofluorescent staining at day 6 of culture, for versican (*A* and *B*), TGF-β (*C* and *D*), both merged (*E* and *F*), TβRII (*G* and *H*), and phospho-Smad2/3 (*I* and *J*) of *Prx1*-Cre/*Vcan*$^{+/+}$ (*A*, *C*, *E*, *G*, and *I*) and *Prx1*-Cre/*Vcan*$^{flox/flox}$ (*B*, *D*, *F*, *H*, and *J*). *Versican is immunostained strongly in the perinodular region and moderately* in the internodular region in *Prx1*-Cre/*Vcan*$^{+/+}$ (*A*), whereas it is immunostained very

faintly in *Prx1*-Cre/*Vcan*$^{flox/flox}$ (*B*). TGF-β is mainly localized in the perinodular regions in *Prx1*-Cre/*Vcan*$^{+/+}$ similar to versican (*C*), whereas it is immunostained diffusely at a substantially lower intensity in *Prx1*-Cre/*Vcan*$^{+/+}$ (*D*). When merged, both verican and TGF-β are well co-localized in the perinodular region (*E*). TβRII is immunostained mainly in the perinodular region in both *Prx1*-Cre/*Vcan*$^{+/+}$ (*G*) and *Prx1*-Cre/*Vcan*$^{flox/flox}$ (*H*) micromass. In addition, it is immunostained rather diffusely in *Prx1*-Cre/*Vcan*$^{flox/flox}$ (*H*). Phospho-Smad2/3 is immunostained in the nuclei of perinodular cells strongly and in chondrocytes in the nodules moderately in *Prx1*-Cre/*Vcan*$^{+/+}$ micromass (*I*). In contrast, it is immunostained moderately in the nuclei of chondrocytes in the nodules and weakly in the perinodular cells in the *Prx1*-Cre/*Vcan*$^{flox/flox}$ micromass (*J*).

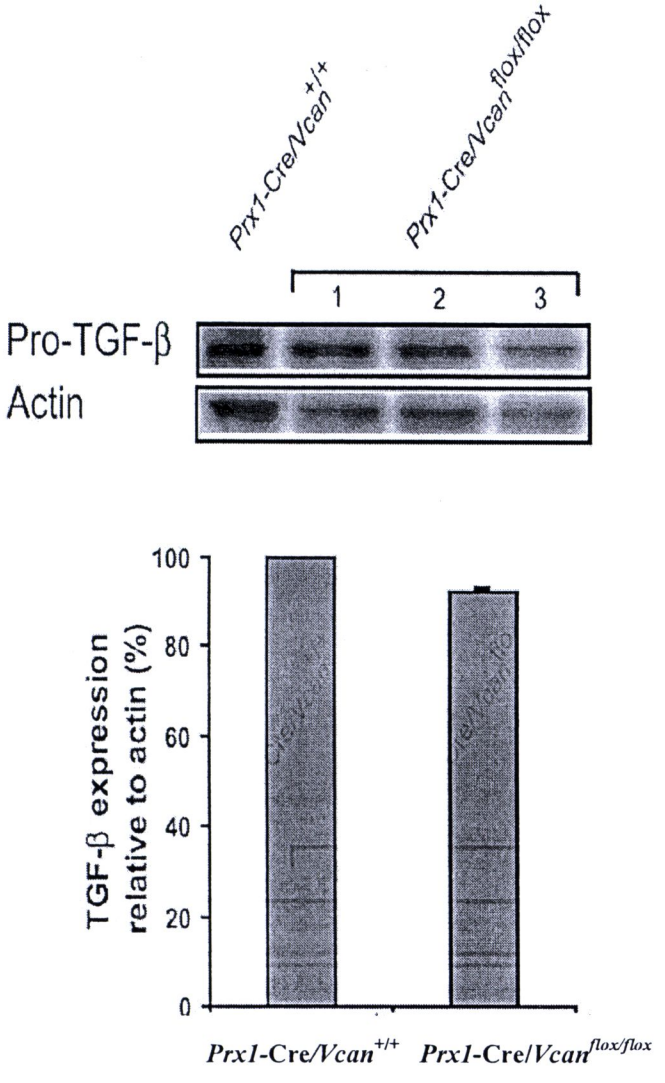

Figure 3.35 Western blot analysis of TGF-β in micromass. Top panels represent Pro-TGF-β together with actin. The graph shows the band density measured by Image J. The expression levels of TGF-β of *Prx1*-Cre/*Vcan*$^{flox/flox}$ (n=3) standardized by actin are shown as percent of *Prx1*-Cre/*Vcan*$^{+/+}$.

3.8 Versican localizes TGF-β in the extracellular matrix

Co-localization of versican and TGF-β in *Prx1*-Cre/*Vcan*$^{+/+}$ micromass and diffuse patterns of TGF-β in the absence of versican in the *Prx1*-Cre/*Vcan*$^{flox/flox}$ micromass strongly suggest a direct binding of versican to TGF-β or its complex. Versican contains at least three functional domains: the G1 domain that binds hyaluronan, the G3 domain that binds various ECM molecules, and CS chains. To investigate whether CS chains are necessary for localizing TGF-β in the ECM, *Prx1*-Cre/*Vcan*$^{+/+}$ micromass was treated with chondroitinase ABC for 48 h before immunostaining. As shown in figure 3.36, in the micromass treated with chondroitinase ABC, versican remained in the areas surrounding the nodules, confirming that CS chains are not essential for incorporation of versican in the ECM. TGF-β also similarly remained in the areas surrounding the nodules. When merged, these molecules were well co-localized in the perinodular region, even after ablation of CS chains. These observations indicate that versican without CS chains may retain the function of localizing TGF-β.

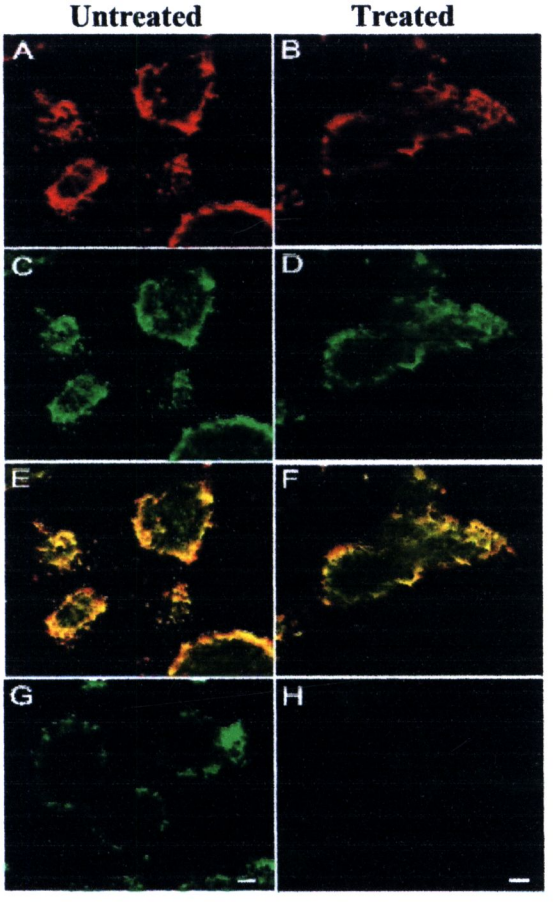

Figure 3.36 Immunofluorescent staining of versican (*A* and *B*) and TGF-β (*C* and *D*) of *Prx1*-Cre/*Vcan*$^{+/+}$ micromass untreated (*A*, *C*, and *E*) and treated with chondroitinase ABC for 48 h before fixation (*B*, *D*, and *F*). The areas immunostained for versican become diffuse by the treatment, although versican essentially remains in the perinodular region (*B*). The areas immunostained for TGF-β become diffuse by the treatment, concomitantly with versican. Merged images are shown (*E* and *F*). Immunostaining for CS chains that confirm ablation of CS is shown (untreated (*G*) and treated (*H*)). *Scale bars*, 15μm. Immunofluorescent staining was performed at least three times, with essentially the same results.

3.9 The phytochemical profiles of the hexane fractions were determined by HPLC

It has been indicated that murine versican was 89% identical to human versican at the amino acid level (40). Hence, the anomaly seen in mouse models may display many of the same behavioral and pathological features seen in human. As previously mentioned, the conditional deletion of versican resulted in joint deformities, thus it might later make mice suffer from this abnormalities as usually seen in joint diseases.

Taking into consideration, rheumatoid arthritis (RA) is one of the common joint disease that primarily affects the joints and results in the progressive destruction of articular structures, particularly cartilage and bone. One of the most prevalent events during pathogenic progression of RA is the hyperplasia of synovial fibroblasts (SFs) of the synovial membranes. SFs in the most superficial lining layer of the hyperplastic RA synovium have been indicated to play an important role in the pathogenesis of RA (239). During the pathological events in RA, the activated synovial fibroblasts in the lining layer of the synovial membrane invade deeply into the articular cartilage and bone, and release several cytokines or MMPs that in turn contribute to cartilage deterioration and joint destruction (21-26). Reportedly, several studies have indicated that *A. galanga* has a potential anti-rheumatic activities (27, 28, 226), however, the precise action of the extract on arthritic diseases is not yet fully understood. Hence, the inflammatory model was established as a clinical study for investigation the effects of *A. galanga* extracts on the expression of genes involved in catabolic activities in an IL-1β-induced human SFs. *A. galanga* extracts were prepared as described in material and methods. All 4 fractions of the extracts were

used as plant materials. The phytochemical profiles of the hexane fractions were determined by HPLC as demonstrated in figure 3.37.

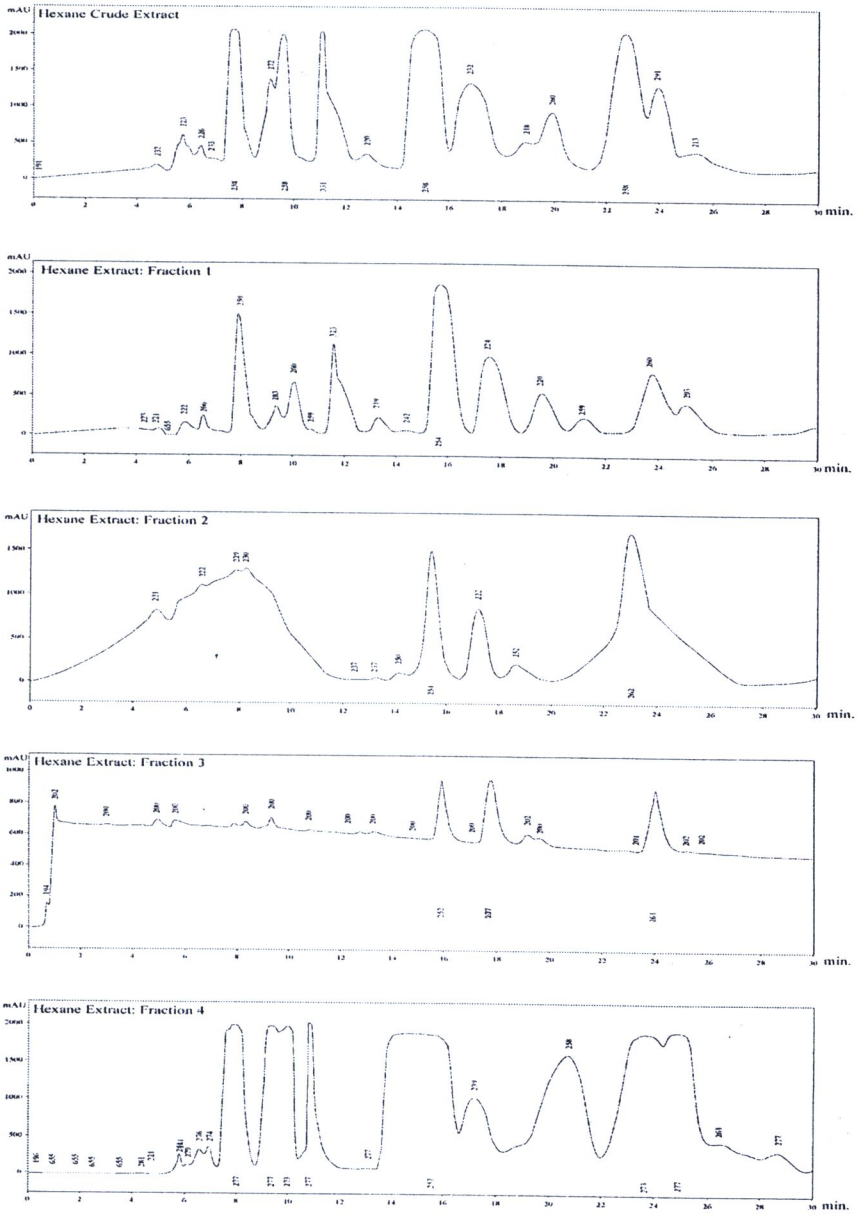

Figure 3.37 HPLC-chromatograms of *A. galanga* extracts. Crude, fraction1, 2, 3, 4 of hexane extract profiles are shown, respectively. Each fraction was applied to a C18 column and eluted with CH_3CN:H_2O (20:80) at a flow rate of 1 ml/min. The fraction profile was monitored using a diode array detection system. The number at an individual peak represents the monitor wavelength.

3.10 Effect of *A. galanga* hexane extracts on IL-1β-reduced gelatinases production

MMP-2 is involved in the pathogenesis of RA by supporting the invasion of microvascular basement membrane and the interstitium (240, 241), and is activated by IL-1β (242). In order to test whether *A. galanga* hexane extracts have the ability to suppress the expression of metalloproteinases, which are highly expressed in arthritic joints, gelatin zymography was performed. Human synovial fibroblasts spontaneously produce small amounts of MMP-2. When confluent synovial fibroblasts were treated with IL-1β (10 ng/ml) for 24 h, the level of MMP-2 in the conditioned medium showed a small increase compared to the untreated control cells. The *A. galanga* extracts of hexane fractions 1-3 could not suppress the IL-1β-induced MMP-2 production (figure 3.38-3.40), in contrast to the extract from fraction 4, which showed a strong decrease compared with fractions 1-3, figure 3.41. The decrease of cell viability by *A. galanga* extracts of hexane fractions 1-3 started at 10 μg/ml, whereas the extract of hexane fraction 4 at 50 μg/ml exhibited that of fractions 1-3, as indicated in figure 3.42 and 3.38-3.41.

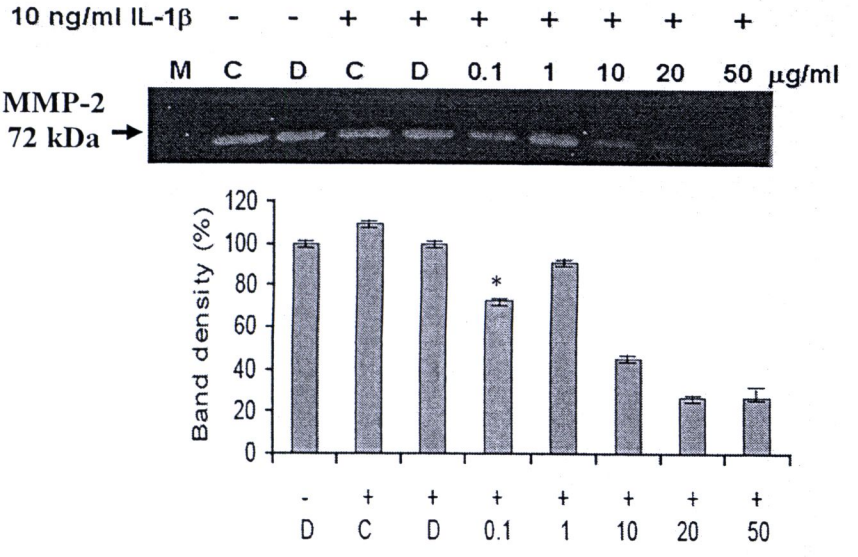

Figure 3.38 Effect of *A. galanga* extracts, fractions 1, on the production of MMP-2. The band density was quantified by Image J. M; protein marker, C; control, D; 0.01 %DMSO. * Denoted *P* value < 0.01.

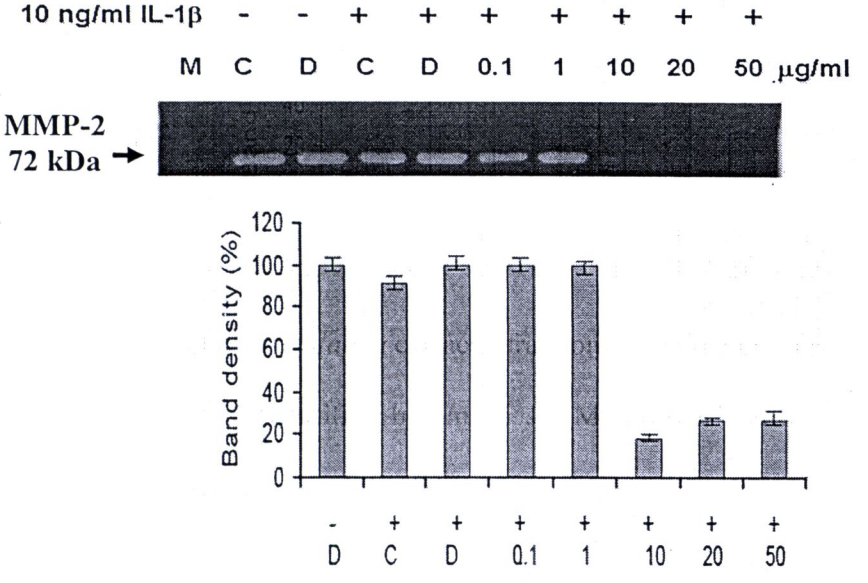

Figure 3.39 Effect of *A. galanga* extracts, fractions 2, on the production of MMP-2. The band density was quantified by Image J. M; protein marker, C; control, D; 0.01 %DMSO.

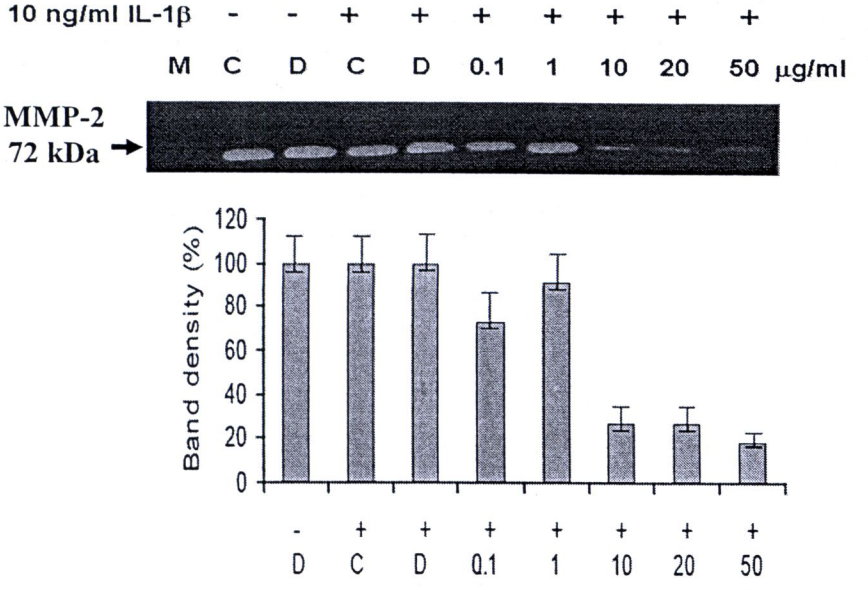

Figure 3.40 Effect of *A. galanga* extracts, fractions 3, on the production of MMP-2. The band density was quantified by Image J. M; protein marker, C; control, D; 0.01 %DMSO.

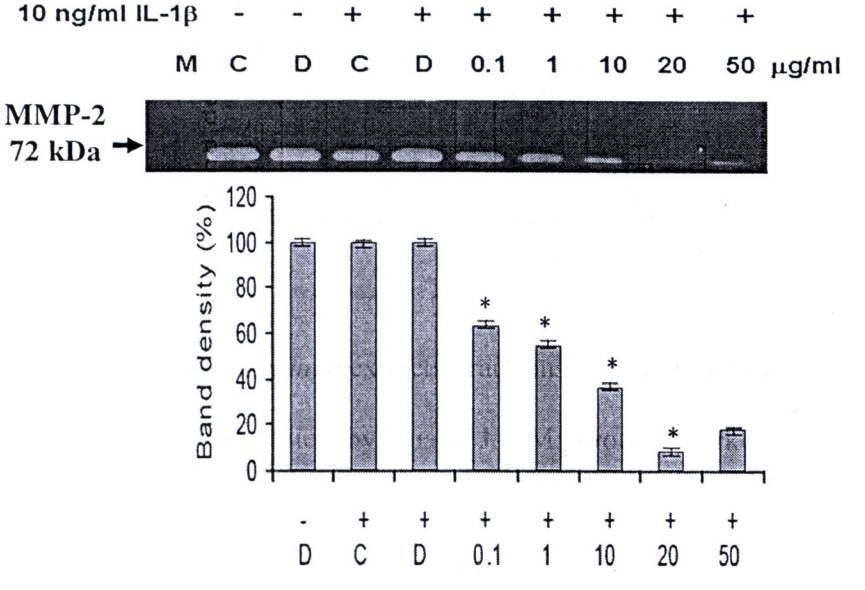

Figure 3.41 Effect of *A. galanga* extracts, fractions 4, on the production of MMP-2. The band density was quantified by Image J. M; protein marker, C; control, D; *0.01 %DMSO. * Denoted P value < 0.01.*

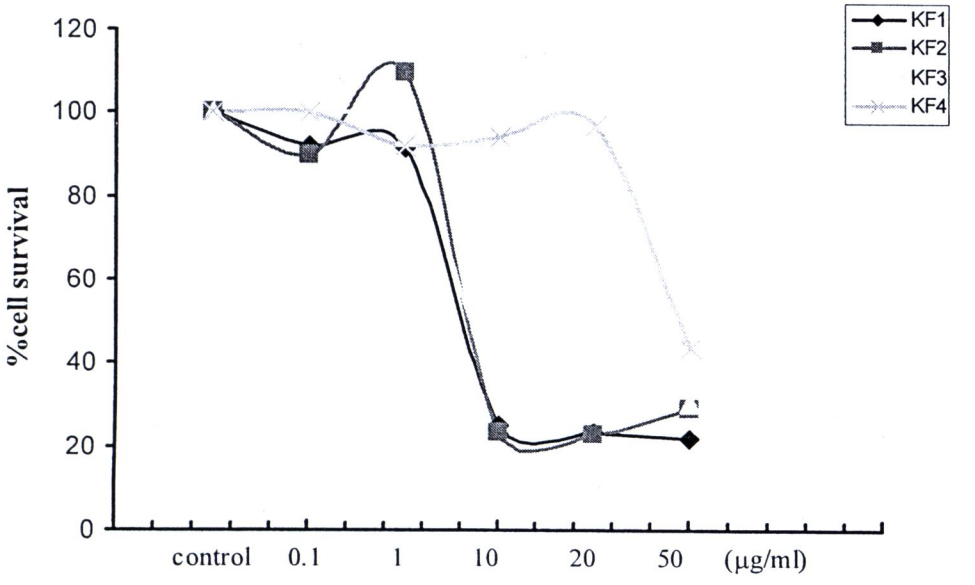

Figure 3.42 Viability of human synovial fibroblasts treated with *A. galanga* extracts; fraction 1-4. KF1; fraction 1, KF2; fraction 2, KF3; fraction 3, KF4; fraction 4.

3.11 Effect of *A. galanga* hexane extracts on IL-1β-reduced gelatinases expression

The effects of *A. galanga* extracts on the IL-1β-induced production of gelatinase gene expression by semi-quantitative RT-PCR were further investigated. As shown in figure 3.43, when confluent human synovial fibroblasts were treated with IL-1β (10 ng/ml) for 24 h, the expression of MMP-9 was decreased at 1 and 10 μg/ml treatments of fraction 1 and 4, respectively. However, MMP-2 expression was not decreased after the treatments.

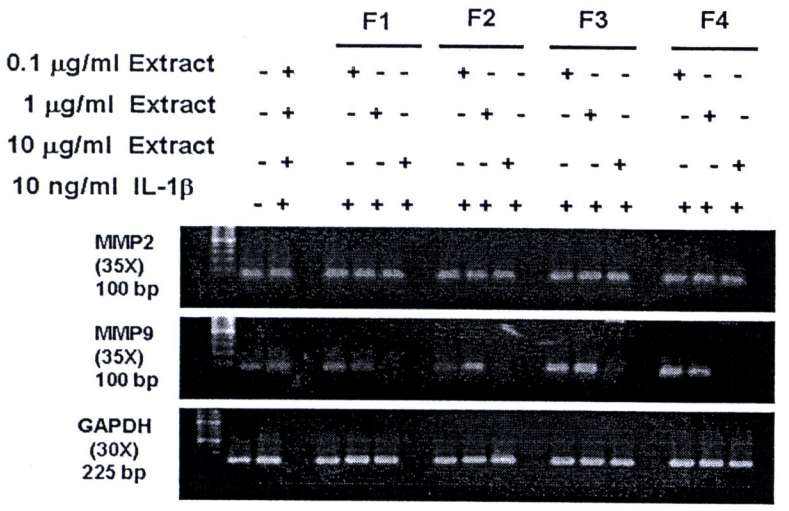

Figure 3.43 Effect of *A. galanga* extracts, fractions 1-4, on gelatinases (MMP-2 and MMP-9) expression. Confluent synovial fibroblasts were cultured with IL-1β (10 ng/ml) in the presence or absence of the *A. galanga* extracts as indicated for 24 h, the cells were collected for RNA extraction, and semi-quantitative RT-PCR using specific primers was performed. F1; fraction 1, F2; fraction 2, F3; fraction 3, F4; fraction 4.

3.12 Effect of *A. galanga* hexane extracts on the IL-1β-induced COX-2 and MMPs expression

Due to the reduction effects on gelatinase expression, we next examined the other proteinases (MMP-1, -3, -13) and COX-2 gene expression, which are associated with extracellular matrix degradation, and is marker of tissue inflammation (243, 244), respectively. Using semi-quantitative RT-PCR, IL-1β slightly stimulated the expression of COX-2, MMP-1, -3, -13 mRNA, figure 3.44. Co-treatment of the cells with *A. galanga* hexane extract fraction 4 at 10 μg/ml inhibited the IL-1β induced COX-2, MMP-1, -3, -13 expression.

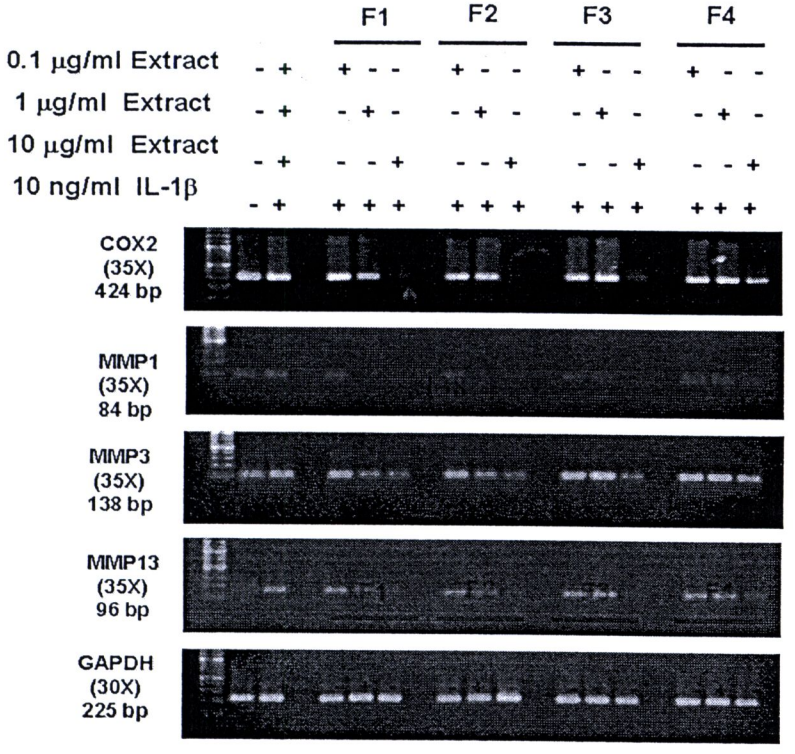

Figure 3.44 Effect of *A. galanga* extracts, fractions 1-4, on COX-2 and proteinases (MMP-1, -3, -13) expression. Confluent synovial fibroblasts were cultured with IL-1β (10 ng/ml) in the presence or absence of the *A. galanga* extracts as indicated for 24 h, the cells were collected for RNA extraction, and semi-quantitative RT-PCR using specific primers was performed. F1; fraction 1, F2; fraction2, F3; fraction 3, F4; fraction 4.